

AD-A042 244

STANFORD UNIV CALIF INTEGRATED CIRCUITS LAB  
OXIDATION AND EPITAXY.(U)

F/G 20/12

UNCLASSIFIED

MAY 77 R W DUTTON, D A ANTONIADIS, J D MEINDL  
TR-5021-1

NL

| OF |  
AD  
A042244



ADA 042244

# INTEGRATED CIRCUITS LABORATORY

STANFORD ELECTRONICS LABORATORIES

DEPARTMENT OF ELECTRICAL ENGINEERING

STANFORD UNIVERSITY · STANFORD, CA 94305



## Oxidation and Epitaxy.

by

10  
R.W. Dutton,  
D.A. Antoniadis,  
J.D. Meindl,  
T.I. Kamins  
K.C. Saraswat  
B.E. Deal

and

J.D. Plummer

14  
MR-5021-1



9  
Technical Report No. 5021-1

11  
May 1977

12  
58p.

This work was supported under DARPA contract DAA-B07-75-C-1344.

### DISTRIBUTION STATEMENT A

Approved for public release;  
Distribution Unlimited

to Sta. Univ.  
(checked contract)

409117

DDC FILE COPY

A PROGRESS REPORT ON  
PROCESS MODELING OF  
SILICON EPITAXY AND OXIDATION

R. W. Dutton  
D. A. Antoniadis  
J. D. Meindl  
T. I. Kamins  
K. C. Saraswat  
B. E. Deal  
J. D. Plummer

ACCESS: for	
NTIS	White Section <input checked="" type="checkbox"/>
DDC	Buff Section <input type="checkbox"/>
UNANNOUNCED	<input type="checkbox"/>
JUSTIFICATION	
Per DDC Form 57	
BY on file	
DISTRIBUTION/AVAILABILITY CODES	
Dist. and/or SPECIAL	
A	

PREFACE. This technical report contains a progress summary of recent activities in IC process modeling of silicon epitaxy and oxidation. The report builds from the most fundamental process models and ends with details of work in progress. Further details appear in technical reports under DARPA contracts DAA-B07-75-C-1344 and DAA-B07-77-C-2684.

ABSTRACT. The first order process models for silicon epitaxy and oxidation are described. Epitaxial dopant inclusion, autodoping and transient effects are discussed, and experimental results are presented. Silicon orientation, surface doping, and ambient effects are considered for silicon-oxidation rates.

## 1. INTRODUCTION

Epitaxy and oxidation are two critical steps in IC technology. Process models date back to the mid-1960's. Epitaxy often controls bipolar circuit performance and yields. Oxide growth is essential in all IC technologies, and segregation frequently dominates fabrication limits and the process control of surface effects. The following sections will review the basic models and introduce considerations for more recent experimental work.

## 2. SILICON EPITAXY

### 2.1 Introduction

There is an extensive literature on the chemistry and reactor dynamics of silicon epitaxy [1] and polycrystalline deposition [2]. The recent advent of low-pressure CVD systems will undoubtedly add substantially to this body of knowledge [3].

The focus of this discussion is on process modeling for silicon epitaxy in a horizontal reactor [4]. This emphasis is based on the experience at Stanford University and, in large part, on that of technologists using commercial equipment. Figure 1 is a schematic of a typical reactor. Table 1 describes the various source gases and their functions, and Table 2 summarizes the key features of several silicon gaseous sources. Table 3 presents a typical reactor sequence used during epitaxial silicon growth. The following sections will elaborate on the fundamental models that describe the kinetics of silicon growth, dopant inclusion, and transient system response.

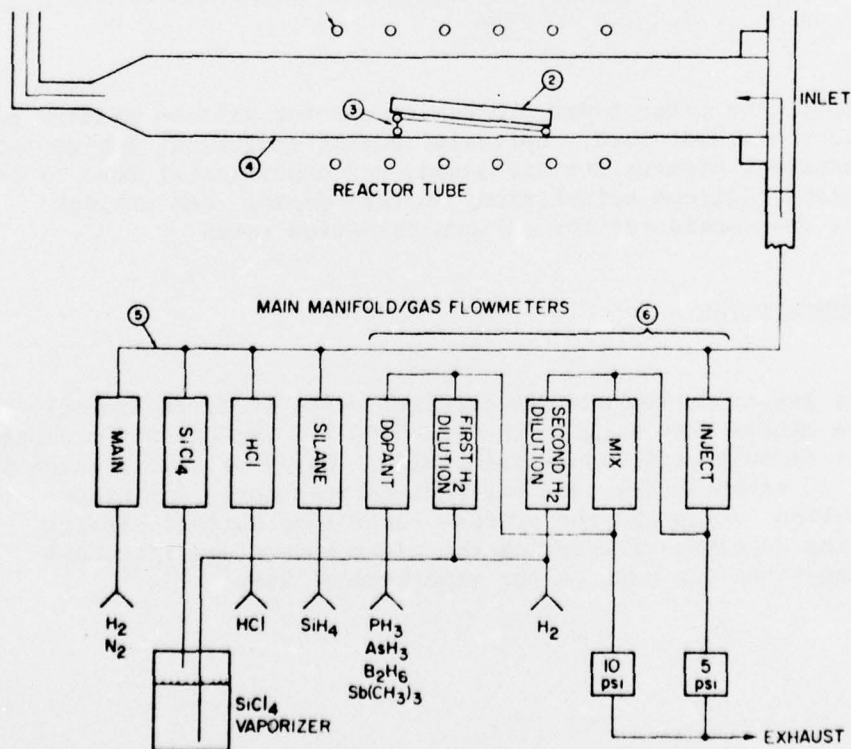


Fig. 1. Schematic of the horizontal epitaxial reactor.



Table 1

## GASES USED IN EPITAXIAL DEPOSITION

Gas	Function	Comments
$N_2$	main flow	Purges out explosive/poisonous gases prior to opening the reactor tube to air
$H_2$	main flow	Most common ambient for growth or epitaxial layers
$SiCl_4$	Si source	Common liquid Si source Vaporized in an $H_2$ bubbler Corrosive vapor
$SiH_4$	Si source	Common gaseous Si source Pyrophoric gas
HCL	Si etchant	Most common Si etchant used for substrate preparation Corrosive poison gas
$PH_3$	Si dopant	Most common phosphorous source for doping epitaxial silicon Flammable poison gas
$AsH_3$	Si dopant	As $PH_3$
$Sb(CH_3)_3$	Si dopant	A liquid antimony source used as a vapor at a concentration of a few hundred ppm in $H_2$ Used because $SbH_3$ is unstable Poisonous vapor
$B_2H_6$	Si dopant	As $PH_3$

Table 2  
SOURCES OF SILICON IN EPITAXY

Source	Typical Conditions		Comments	Reference
	Temperature (°C)	Rate (μ/min)		
SiH <sub>4</sub>	1000 to 1050	0.2 to 1.0	Pure gaseous source Pyrophoric gas Low-temperature deposition Low autodoping Moderate growth rates Surface quality sensitive to O <sub>2</sub>	1,3,4,5,8 9,10,12 13
SiCl <sub>4</sub>	1150 to 1200	0.5 to 1.5	Corrosive liquid source High-temperature deposition Moderate autodoping, outdiffusion Moderate-high growth rates Most common source for linear bipolar integrated circuits Easy to obtain good crystal quality on thick layers	1,2,6,11 13,14 15
SiHCl <sub>3</sub>	1150 to 1200	1.0 to 10	Corrosive liquid source High-temperature deposition Moderate autodoping Very high growth rates Most common source of poly-Si dielectric isolation Very high purity epitaxial layers used in high-voltage devices	1,7 20 16,17
SiH <sub>2</sub> Cl <sub>2</sub>	1050 to 1100	≥1.0	Gaseous source at 7 psi Properties: intermediate SiCl <sub>4</sub> , SiH <sub>4</sub>	1,37
SiBr <sub>4</sub>	---	---	Rarely used source	18
Si(CH <sub>3</sub> ) <sub>4</sub>	1150	0.4	Rarely used source	19

Table 3  
TYPICAL EPITAXIAL GROWTH CYCLE

Step	Time	Temperature	Gas Concentration	Comment
N <sub>2</sub> purge	2'	R.T.	---	Purge out O <sub>2</sub>
H <sub>2</sub> purge	2'	R.T.	---	Charge to H <sub>2</sub> ambient
Heat	2'	1200°C	---	In H <sub>2</sub> ambient
HCL etch	2'	1200°C	1%	Etch 0.26 μ of silicon
H <sub>2</sub> purge	2'	to 1050°C	---	To lower temperature and remove HCL
Growth	8'20"	1050°C	0.05% SiH <sub>4</sub> 0.3 ppb PH <sub>3</sub>	Growth of 5 μ, 1 Ω-cm P-doped Si layer
H <sub>2</sub> purge	1'	1050°C	---	Purge reactants prior to cooling
Cool	4'	R.T.	---	In H <sub>2</sub> ambient
N <sub>2</sub> purge	2'	R.T.	---	Before opening to air

## 2.2 Film growth

For the kinetics of film growth, the silicon source gas reacts and decomposes as described by a typical equation for silane,



The silicon growth rate is proportional to the partial pressure of silane,

$$V = K_I (\text{SiH}_4)_I \quad (2)$$

where  $V$  is the growth rate,  $K_I$  is the surface-reaction rate constant, and the subscript denotes the surface quantities. For halide-bearing source gases, there are reactive conditions whereby silicon etching occurs; however, for model simplicity, these source gases will not be considered because of the complexity of the multispecies reaction.

Equation (2) describes growth only under the conditions of surface-reaction control; that is, surface reaction is the limiting step. Figure 2 is a typical Arrhenius plot for silane growth vs inverse temperature with gas partial pressure as a parameter [4]. The silane concentrations are those of the turbulent gas stream.

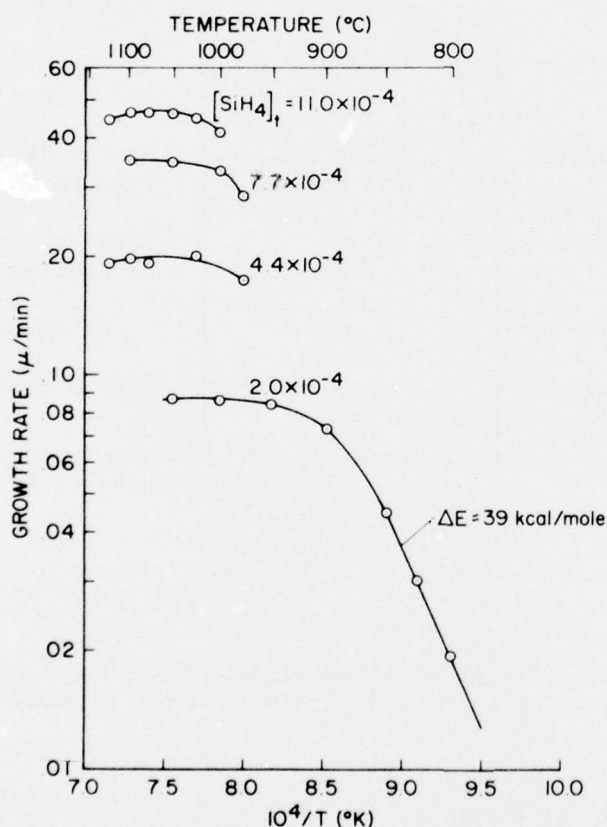


Fig. 2. Arrhenius plot of  $\text{SiH}_4$  growth rate.



Figure 3 is a cross section of the reactor. A boundary layer [5] (often labeled a "stagnant" layer) exists between the turbulent gas and reactive wafer interface I; also shown are plots of reactant gas species under two limiting cases.

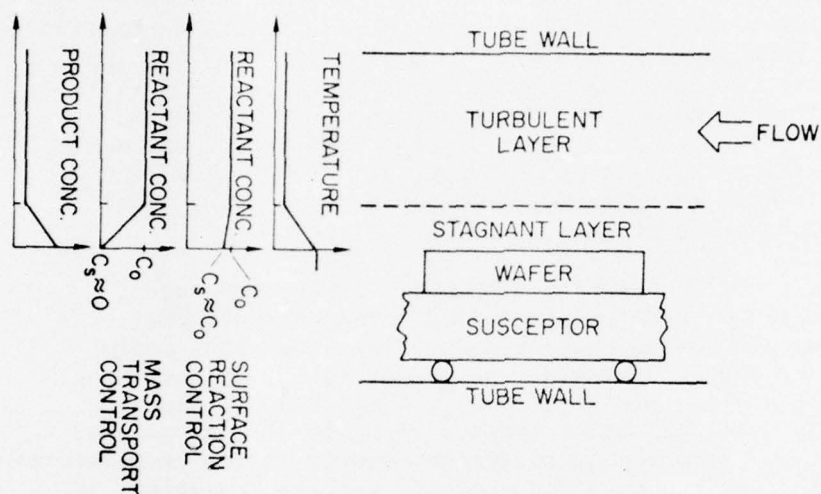


Fig. 3. Cross section of horizontal reactor with thermal and chemical profiles during growth.

Epitaxial growth proceeds by the following steps:

- (1) mass transfer of the reactant molecules (such as  $\text{SiH}_4$ ) by diffusion from the turbulent-layer reservoir across the boundary layer to the silicon surface.
- (2) adsorption of reactant atoms on the surface
- (3) one or more chemical reactions at the surface
- (4) desorption of product molecules (such as  $\text{H}_2$ )
- (5) mass transfer of the product molecules by diffusion through the boundary layer, back to the turbulent layer
- (6) lattice arrangement of the adsorbed silicon atoms (may occur as part of 3)

Concentration gradients across the boundary layer are such that there is a diffusion flux of product molecules away from the surface. The turbulent layer is depicted as having no concentration or temperature gradient.

The overall deposition rate is determined by the slowest of processes (1 to 6 above). The expected temperature dependence of the growth rate varies markedly for different controlling mechanisms. If diffusion of either reactant or product across the stagnant layer (so-called mass-transport control) is the slowest part of the reaction, the growth rate would not depend on the temperature to first order. On the other hand, if a surface chemical reaction is the slowest process (surface-reaction rate control), one would expect the deposition rate to have the same temperature dependence as the chemical reaction, which is an exponential function of inverse temperature. Furthermore, because the various silicon sources undergo different chemical reactions with different activation energies, one would expect them to have diverse growth-rate temperature dependences under surface-reaction rate control.

The curve shown in Figure 2 displays a low-temperature reaction region in which surface-reaction rates dominate the growth rate and a high-temperature nonactivated reaction realm in which mass transport dominates the growth rate. One striking feature is that similar plots for  $\text{SiCl}_4$ ,  $\text{SiH}_4$ ,  $\text{SiH}_2\text{Cl}_2$ , and  $\text{SiHCl}_3$  have the same activation energy; (roughly 37 kcal/mole or 1.6 eV/molecule). This common activation energy in the temperature-dependent region implies that the dominant surface "reaction" is step 6; (the lattice arrangement of the silicon atoms). Indeed, the activation energy for surface diffusion of adsorbed silicon atoms on silicon has been measured to be  $36 \pm 6$  kcal/mole [6].

At higher temperatures, growth reaction is nonactivated, suggesting that the slowest process is mass transport of either products or reactants. The rate-limiting step is probably reactant transfer. This hypothesis is supported by two considerations. First, in the boundary layer under reactant mass-transport limited conditions, the growth rate is proportional to the diffusion coefficient of the reactant species in hydrogen. This coefficient, in turn, is proportional to the inverse square root of the molecular weight of the reactant molecule. Second, the large temperature gradient in the boundary layer tends to retard the gaseous diffusion of reactants toward the susceptor and to increase the diffusion of products away from the susceptor.

In summary, boundary-layer theory and empirical observations produce the following qualitative results for the epitaxial growth rate of common silicon sources.

- (1) The growth rate indicates two distinct regions, a low-temperature region in which the growth rate fits an Arrhenius plot and a high-temperature region in which the growth rate does not depend on temperature.

(2) In the low-temperature region:

- (a) Activation energy is approximately 37 kcal/mole, a number consistent with the activation energy for surface diffusion of adsorbed silicon atoms.
- (b) Activation energy is independent of source type.
- (c) For low source concentrations, the growth rate is directly proportional to the input silicon source concentration.
- (d) The linear growth rate/source concentration relationship applies at high growth rates only for  $\text{SiH}_4$ . The chloride-containing sources do not obey this relationship because a reverse reaction, HCl etching, occurs [7].

(3) In the high-temperature region:

- (a) The temperature insensitive growth rate is controlled by mass transport of the silicon source from the turbulent layer to the silicon interface by diffusion.
- (b) For low source concentrations, the growth rate is directly proportional to the input silicon source concentration.
- (c) The growth rates for chloride-containing sources are not linear functions of source concentration at high concentrations because of HCl etching.

The changeover between the surface-controlled and mass-transport controlled realms of  $\text{SiH}_4$  deposition can be described by the balancing of molecular fluxes because no reverse reactions complicate the  $\text{SiH}_4$  problem. The growth rate  $V$  is directly proportional to the  $\text{SiH}_4$  concentration at the silicon surface, as given by Eq. (2). The surface-reaction rate constant  $K$  has the characteristic activation energy of 37 kcal/mole and the units of the growth rate (cm/sec) because  $[\text{SiH}_4]_I$  is a unitless ratio of gas flows. The flux of  $\text{SiH}_4$  atoms across the boundary layer  $F_I$  is proportional to the  $\text{SiH}_4$  concentration gradient across the layer, which is the difference between  $\text{SiH}_4$  concentration in the turbulent layer  $[\text{SiH}_4]_T$  and that at the interface  $[\text{SiH}_4]_I$ ,

$$F_I = h(\text{SiH}_4) \left[ [\text{SiH}_4]_T - [\text{SiH}_4]_I \right] \quad (3)$$

where  $h(\text{SiH}_4)$  is the mass-transport coefficient for  $\text{SiH}_4$  and is a temperature-insensitive constant that relates molecular flux to the concentration gradient; it is proportional to the  $\text{SiH}_4$  diffusion coefficient in  $\text{H}_2$  and is inversely proportional to the boundary-layer thickness. The flux of silicon atoms being incorporated into the lattice is

$$F_2 = N_{Si} V \quad (4)$$

in which  $N_{Si}$  is the atomic density of silicon,  $N_{Si} = 5.0 \times 10^{22} \text{ cm}^{-3}$ . A simultaneous solution of Eqs. (2) through (4) obtains the inter-face silane concentration,

$$[\text{SiH}_4]_I = [\text{SiH}_4]_T \left[ 1 + \frac{N_{Si}}{h(\text{SiH}_4)} K_I \right]^{-1} \quad (5)$$

There are two limiting cases:

Case 1: Surface-reaction control.

At low temperatures,  $K_I$  is small enough so that  $[\text{SiH}_4]_I \approx [\text{SiH}_4]_T$  (See Figure 3). In this case, from Eq. (2),

$$V = K_I [\text{SiH}_4]_T \quad (6)$$

Case 2: Mass-transport control.

At high temperatures,  $K_I$  becomes large, and  $[\text{SiH}_4]_I \approx 0$ ; then from Eqs. (2) and (3),

$$V = \frac{h(\text{SiH}_4)}{N_{Si}} [\text{SiH}_4]_T = K_M [\text{SiH}_4]_T \quad (7)$$

The rate constant for mass-transport control is  $K_M$  (cm/sec).

Although Eqs. (6) and (7) predict a first-order growth-rate dependence on silane concentration, the surface-reaction rate constant  $K_I$  is exponentially dependent on temperature and the mass-transport rate constant  $K_M$  has only a linear dependence on temperature (essentially no dependence over the narrow 1000° to 1100°C range commonly used for  $\text{SiH}_4$  epitaxy).

Experimental  $\text{SiH}_4$  growth rate is plotted vs temperature in Figure 2. The surface-reaction region has an activation energy of  $\Delta E = 39 \text{ kcal/mole}$ . Transfer to the mass-transport region is nearly complete at 1000°C for all growth rates from 0.1 to 0.5  $\mu/\text{min}$ . From 1000°C, the maximum variation observed is only 10%. Figure 4 is a graph of growth rate vs silane concentration for  $T = 1050^\circ\text{C}$ . The slope of the line is the mass-transport rate constant value  $K_M = 7.5 \times 10^{-4} \text{ cm/sec} = 450 \mu/\text{min}$ . These values for activation energy [6] and the rate constant [5] are consistent with the literature.



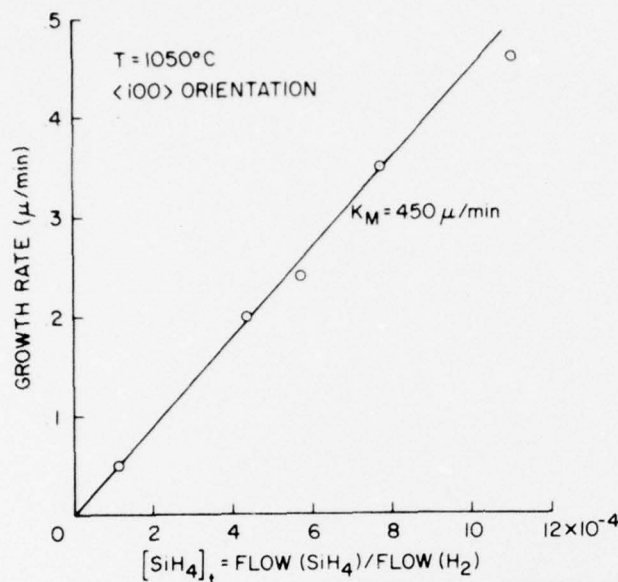


Fig. 4. SiH<sub>4</sub> growth rate vs SiH<sub>4</sub> concentration.

### 2.3 Doping of epitaxial layers

**2.3.1 Injected species.** Epitaxial layers are most commonly doped by the incorporation of a small amount of dopant hydrides (PH<sub>3</sub>, AsH<sub>3</sub>, B<sub>2</sub>H<sub>6</sub>). Phosphine, arsine, and diborane are gaseous sources that can be diluted to the 10<sup>-9</sup> level required for lightly doped epitaxial layers. The doping of SiH<sub>4</sub> epitaxial layers with dopant hydride sources has been described theoretically [8,9]. The dopant is transported across the boundary layer by diffusion as described in the previous section for SiH<sub>4</sub>. The analysis is complicated, however, by the fact that the incorporated dopant is nonuniformly distributed near the surface of the growing layer. The relevant dopant concentrations in the reactor and in the wafer are presented in Figure 5 for PH<sub>3</sub>. The turbulent layer (input) dopant molar concentration [PH<sub>3</sub>]<sub>T</sub> is the flow ratio PH<sub>3</sub>/H<sub>2</sub>. The concentration of phosphine near the surface of the growing epitaxial layer is [PH<sub>3</sub>]<sub>I</sub>. The concentration of incorporated phosphorous atoms near the surface of the layer [P]<sub>I</sub> is higher than the phosphorous concentration deeper in the bulk material [P]<sub>B</sub> [8,9]. All of the incorporated phosphorus is considered to be ionized. The solid-state phosphorous concentrations [P]<sub>I</sub> and [P]<sub>B</sub> have units of (atoms P/atoms Si) and must be multiplied by the atomic density of silicon ( $N_{Si} = 5.0 \times 10^{22}$  atoms/cm<sup>3</sup>) to obtain the conventional doping concentration.

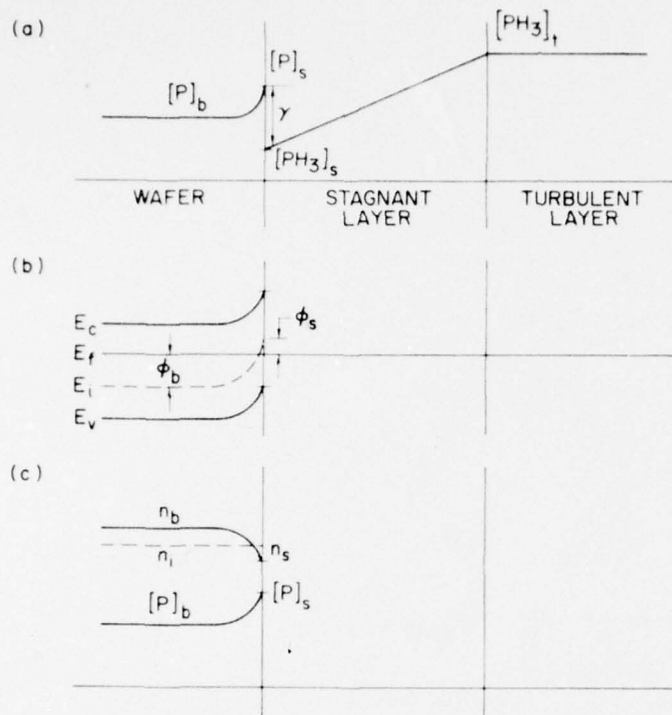


Fig. 5. Dopant concentrations in the reactor and in the wafer.

- (a) Dopant concentrations near an epitaxial interface
- (b) Band bending near a growing silicon surface
- (c) Dopant and free-electron concentrations near a growing silicon surface

The goal of this analysis is to predict the solid-state doping  $[P]_B$  from the turbulent-layer phosphine concentration  $[PH_3]_T$  as a function of temperature and growth rate. The effective segregation coefficient  $\gamma_{EFF}$  relates these two variables as

$$\frac{[P]_B}{[PH_3]_T} = \frac{1}{\gamma_{EFF}} \quad (8)$$

For doping concentrations lower than the concentration of free electrons in silicon at epitaxial temperatures ( $10^{19} \text{ cm}^{-3}$ ), the segregation coefficient is a function of only temperature and growth rate, but not doping level [8]; that is, for a set temperature and growth rate, solid-state doping is a linear function of gas-phase dopant concentration. With respect to the dopant concentrations defined in Figure 5a, Eq. (8) can be expressed as

$$\frac{[P]_B}{[PH_3]_T} = \frac{1}{\gamma_{EFF}} = \frac{[P]_B}{[P]_I} \cdot \frac{[P]_I}{[PH_3]_I} \cdot \frac{[PH_3]_I}{[PH_3]_T} \quad (9)$$

(a)            (b)            (c)

The overall partition coefficient  $\gamma_{EFF}$  can now be evaluated term by term. Ratio (a) on the RHS of Eq. (9) relates the surface and bulk solid-phase dopant levels that may be different because of band bending at the growing silicon surface. Ratio (b) relates the actual solid and gas doping concentrations at the interface. Ratio (c) is essentially a measure of the boundary layer doping gas gradient which is the driving force that provides the required flux of dopant to the surface.

Following the notation in Figure 5 and the derivations of Rodgers [4] and Bloem [8], the expression for an effective segregation coefficient is

$$\frac{[P]_B}{[PH_3]_T} = \frac{1}{\gamma_{EFF}} = \left\{ \frac{\gamma}{\exp \frac{\phi_S - \phi_B}{kT} + \exp \frac{V_C}{V} \left[ 1 - \exp \frac{\phi_S - \phi_B}{kt} \right]} + \frac{h(SiH_4)}{h(PH_3)} [SiH_4]_T \right\}^{-1} \quad (10)$$

where  $\phi_S$  is the surface potential pinned at one-third the gap above the valence band [8],  $\phi_B$  is the bulk Fermi potential, and  $V_C$  is a critical growth rate at which trapping starts to occur. The parameter  $h(PH_3)$  is the phosphine transport coefficient similar to  $h(SiH_4)$ , and the other parameters have their standard meanings. Figure 5 defines the equilibrium segregation term

$$\frac{1}{\gamma} = \frac{[P]_I}{[PH_3]_I} \quad (11)$$

For low growth rates, the effective segregation coefficient is equal to the equilibrium segregation coefficient  $\gamma$ , modified to account for trapping. Reactant incorporation is surface-reaction limited. For high growth rates, the effective segregation coefficient is proportional to the input silane concentration  $[\text{SiH}_4]_T$ . Four limiting cases of Eq. (10) exist as a result of combining the two limiting conditions in the crystal (bulk-surface equilibrium and complete trapping) with the two limits for dopant transport to the crystal (surface reaction and mass transport). These cases are depicted schematically in Figure 6 for an arbitrary donor hydride  $\text{DH}_3$ .

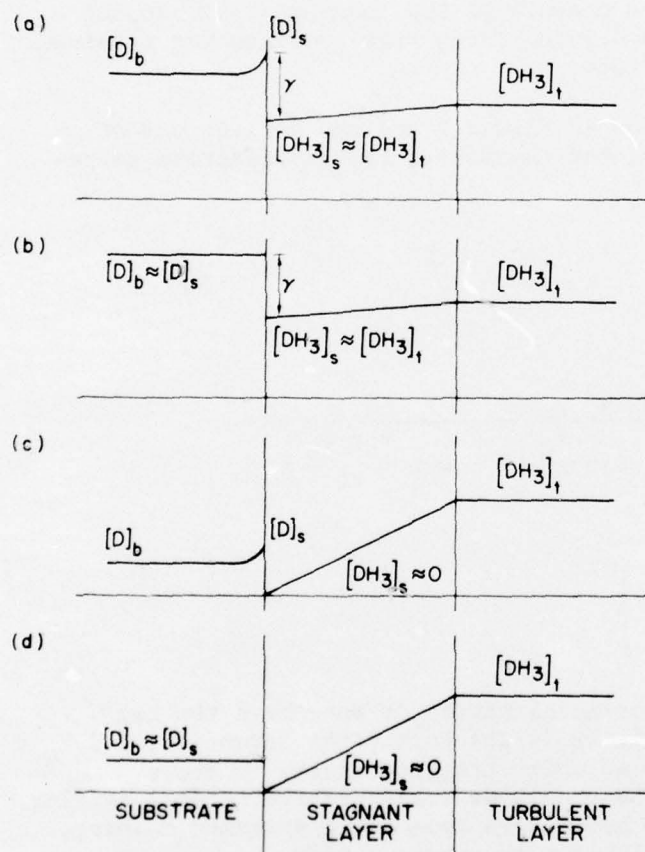


Fig. 6. Limiting-case dopant-concentration profiles for silicon epitaxial layers.



Case 1.

Surface-reaction limited dopant transport and bulk-surface equilibrium conditions would occur during growth at moderately high temperatures, low growth rates, and with a fast diffusing dopant (1150°C, 0.1  $\mu$ /min,  $\text{PH}_3$ ) [9]. In this case, Eq. (10) can be approximated by

$$\frac{[\text{P}]_B}{[\text{PH}_3]_T} = \frac{1}{\gamma_{\text{EFF}}} = \frac{1}{\gamma / \exp \frac{\phi_S - \phi_B}{kT}} \quad (12)$$

The effective segregation coefficient is the equilibrium segregation coefficient modified by band-bending effects.

Case 2.

Surface-reaction limited dopant transport and surface dopant trapping conditions would occur during growth at low temperatures, moderate growth rates, and with a slow diffusing dopant (1000°C, 0.5  $\mu$ /min,  $\text{AsH}_3$ ). The effective segregation coefficient is then the equilibrium segregation coefficient,

$$\frac{[\text{As}]_B}{[\text{AsH}_3]_T} = \frac{1}{\gamma_{\text{EFF}}} = \frac{1}{\gamma} \quad (13)$$

Case 3.

Mass-transport limited dopant delivery and bulk-surface equilibrium conditions would occur during growth at very high temperatures, moderately high growth rates, and with a fast diffusing dopant (1225°C, 2  $\mu$ /min,  $\text{PH}_3$ ). The effective segregation coefficient is determined by mass transport of dopant across the boundary layer. Equation (10) can be approximated as

$$\frac{[\text{P}]_B}{[\text{PH}_3]_T} = \frac{1}{\gamma_{\text{EFF}}} = \frac{1}{[h(\text{SiH}_4)/h(\text{PH}_3)] [\text{SiH}_4]_T} \quad (14)$$

Case 4.

Mass-transport limited dopant delivery and surface dopant trapping conditions would occur during growth at relatively low temperatures, high growth rates, and with a slow diffusion dopant (1050°C, 4  $\mu$ /min,  $\text{AsH}_3$ ). The effective segregation coefficient is given in Eq. (14).

Although all of the growth conditions depicted in Fig. 6 are possible, practical considerations limit  $\text{SiH}_4$  epitaxial growth to the 1000° to 1050°C range and a 0.2 to 1.0  $\mu/\text{min}$  growth rate. At higher temperatures, the  $\text{SiH}_4$  process has the following problems.

- (1) At high growth rates,  $\text{SiH}_4$  tends to decompose in the boundary layer, forming a "cloud" in the reactor that quickly coats the exit end of the reactor tube.
- (2) Silicon deposition on the reactor tube increases for air-cooled tubes.
- (3) Autodoping and outdiffusion begin to become problems.

At temperatures below 1000°C, crystal quality suffers; there is a maximum epitaxial growth rate for every temperature below which polycrystalline deposition occurs. Growth rates below 0.2  $\mu/\text{min}$  are impractical for common 3 to 20  $\mu$  layers because long deposition times are not only wasteful, but lead to excessive out-diffusion. Typical silane-reaction conditions are intermediate, therefore, to the conditions depicted in Figure 6a and 6b. Some surface-dopant trapping is present; an increase in growth rate leads to an increase in solid doping level, all other variables held constant.

The effective segregation coefficient has been measured experimentally over a wide range of conditions. Bulk doping concentration vs monotomic gas-phase dopant concentration is presented in Figure 7 for a combination of different dopant sources, silicon sources, growth rates, and temperatures. The doping concentration is calculated as the effective flow ratio of dopant gas to main hydrogen flow. With reference to the reactor in Figure 1, this ratio is

$$[\text{DX}] = \frac{f(\text{dopant})}{f(\text{dopant}) + f(1\text{st } \text{H}_2)} \cdot \frac{f(\text{mix})}{f(\text{mix}) + f(2\text{nd } \text{H}_2)} \cdot \frac{f(\text{inject})}{f(\text{main})} \quad (15)$$

where  $f$  is the flow in liters per minute. The concentration in the right-hand scale is the normal concentration per cubic centimeter divided by  $N_{\text{Si}}$ . All the dopants have higher concentrations in the bulk than in the gas phase by a factor of 10 to 200 and have approximately the same effective partition coefficient ( $\approx 0.01$ ) except for  $\text{AsH}_3/\text{SiH}_4$  at 1050°C and  $(\text{CH}_3)_3\text{Sb}/\text{SiH}_4$ .

The fact that the effective partition coefficients are independent of growth rate, temperature, and even silicon source for  $\text{PH}_3$  and  $\text{B}_2\text{H}_6$  suggests a surface-reaction limited process with

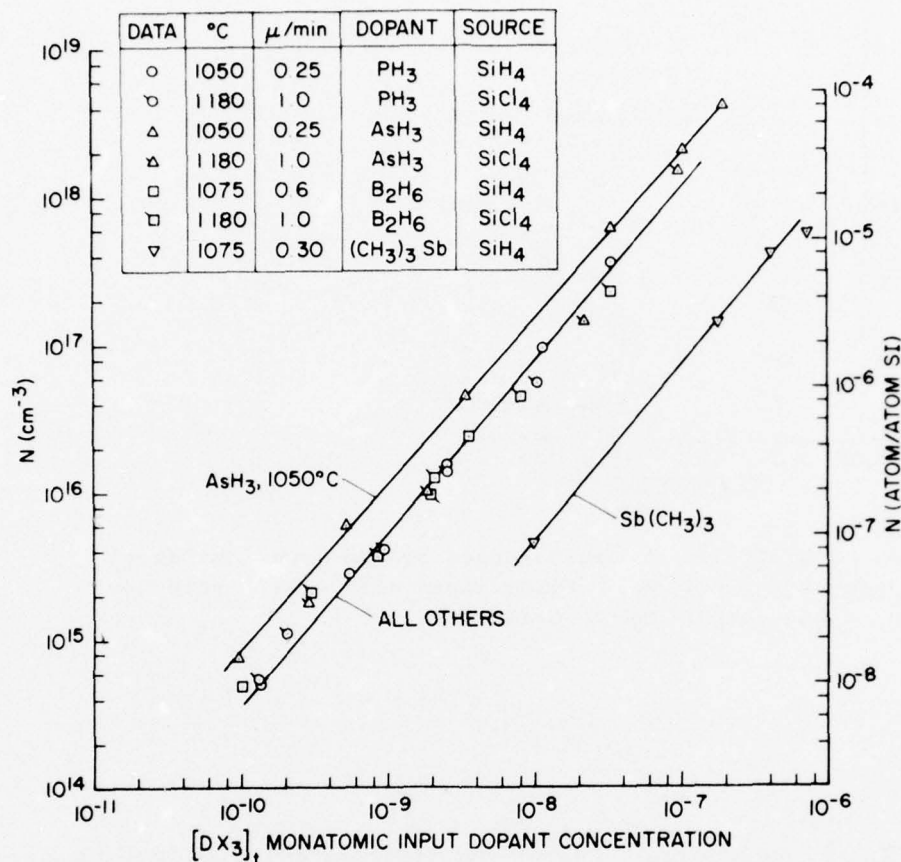


Fig. 7. Solid-state doping vs gas-phase dopant concentration for various dopant sources, silicon sources, and temperatures.

bulk-surface equilibrium (Figure 6(a)). Trapping is not present to any appreciable degree for PH<sub>3</sub>/SiH<sub>4</sub> because of the low 0.25  $\mu$ /min growth rate. For PH<sub>3</sub>/SiCl<sub>4</sub>, B<sub>2</sub>H<sub>6</sub>/SiH<sub>4</sub>, the high growth temperatures (1075° to 1180°C) establish surface-bulk equilibrium. There is some trapping in the 1050°C AsH<sub>3</sub>/SiH<sub>4</sub> system relative to the 1180°C AsH<sub>3</sub>/SiCl<sub>4</sub> system, as evidenced by the higher solid doping concentration for a given input arsine concentration.

The trapping phenomenon in AsH<sub>3</sub>/SiH<sub>4</sub> epitaxial layers has been considered as a function of temperature and growth rate. According to Eq. (10), doping should decrease as temperature ( $V_C$ ) increases in the presence of trapping. This trend is verified for three growth rates in Figure 8. All the curves begin to flatten out at 1025°C, indicating that trapping is nearly complete,  $[As]_B \approx [As]_I$ .

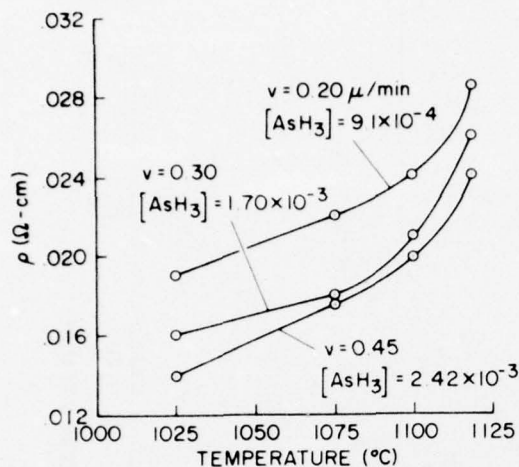


Fig. 8. Resistivity of arsine-doped silane-grown epitaxial layers as a function of temperature with growth rate and arsine concentrations as parameters.

2.3.2 Autodoping. One of the limiting and most important considerations in epitaxial deposition is the movement of substrate impurities into epitaxial layers. Two components are considered -- outdiffusion (movement caused by solid-state thermal diffusion in silicon) and autodoping (extra movement of substrate doping into an epitaxial layer, which cannot be explained by diffusion effects). The following dopant fluxes from a wafer into an epitaxial layer must be considered:

- (1) dopant "evaporated" from the back of the wafer, which mixes into the turbulent layer
- (2) dopant "evaporated" from the front of the wafer into the boundary layer
- (3) dopant that outdiffuses from the substrate as a result of thermal diffusion alone.

For standard buried-collector bipolar processing, a moderately doped ( $10^{15}$  to  $10^{16} \text{ cm}^{-3}$ ) epitaxial layer is grown over localized



$N^+$  buried layers. The backside of the wafer is usually masked during the buried-layer diffusion to eliminate this autodoping source. The wafer is then subjected to very high temperature-time cycles to produce junction isolation; in this case, the sealed-wafer backside does not provide an autodoping source, and frontside autodoping is dominated by outdiffusion from the high-temperature isolation step. Consequently, for standard buried-collector processing, outdiffusion can explain dopant migration from the buried layer into the epitaxial layer [10].

For low-temperature silane epitaxial growth, especially when high-temperature processing steps do not follow, there is a definite movement of dopant into the growing layer from the substrate that cannot be explained by outdiffusion. Figure 9 is the profile of an undoped epitaxial layer grown with silane (1100°C, 0.4  $\mu$ /min) on an arsenic-doped substrate.\* For the 10 min period at high temperature, the diffusion length for arsenic is  $\sqrt{DE} = 0.041 \mu$ . The profile solution for outdiffusion [10] is

$$N(\text{epi}) = \frac{1}{2} N(\text{substrate}) \operatorname{erfc} \left( \frac{x}{2 \sqrt{Dt}} \right) \quad (16)$$

in which  $x$  is the distance into the epitaxial layer measured from the interface. The calculated outdiffusion curve is graphed in Figure 9.

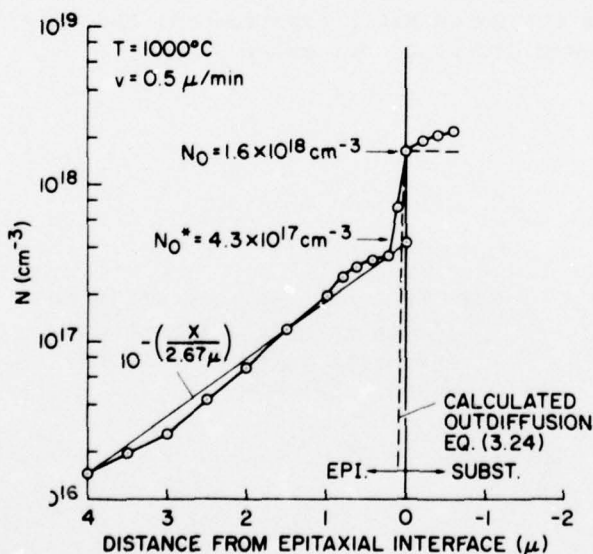


Fig. 9. Autodoping profile for an intrinsic silane-grown epitaxial layer on an arsenic-doped substrate.

\*All profile measurements were made using the spreading-resistance probe technique.

In this case, the dopant movement (here called "autodoping") is dominant over the "outdiffusion" term. Because, for this experiment, the arsenic-doped "wafer" was actually an arsenic-doped epitaxial layer deposited on a lightly boron-doped wafer, the sole component of autodoping contributing to the measured profile was evaporation from the front of the wafer into the growing layer. A well-known feature of the frontside evaporation solution is that the evaporation rate is proportional to the surface concentration [11]. As the surface concentration, resulting from autodoping decreases, the evaporation rate decreases which, in turn, reduces concentration in the growing layer; the doping profile is a simple decaying exponential extrapolating back to an effective surface concentration  $N_0^*$  which is determined empirically for a given dopant, silicon source, and set of growth conditions. For arsenic-silane in Figure 9, the profile is close to exponential, dropping a factor of 10 every 2.67  $\mu$ .

This behavior has also been measured in layers grown at higher temperatures with  $\text{SiCl}_4$ . Figure 10 shows the measured autodoping tail of a boron-doped substrate into an undoped epitaxial layer grown with  $\text{SiCl}_4$  at  $1180^\circ\text{C}$  and  $1.0 \mu/\text{min}$ . Here, the calculated outdiffusion is comparable to the autodoping. Outdiffusion is much more prominent than in the previous case because of the higher growth temperature and the higher diffusivity of boron relative to arsenic. Again, an exponential fit is within experimental error. The curve decays a factor of 10 every 0.86  $\mu$ . If a substantial subsequent heating step such as diffusion isolation had been done to the substrates used in the boron  $\text{SiCl}_4$  experiments, the outdiffusion tail would have become dominant over autodoping.

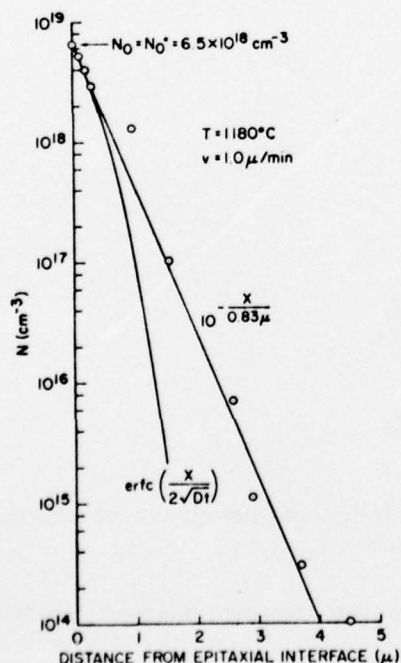


Fig. 10. Autodoping profile for an intrinsic silane-grown epitaxial layer on a boron-doped substrate.

One immediate conclusion that can be drawn from a comparison of Figures 9 and 10 is that the dopant species is a very important consideration. One would expect a priori the slow-diffusing dopant, As, grown at the lower temperature to have much less autodoping than the fast-diffusing dopant, B, grown at the higher temperature. Because the opposite is true, arsenic must be a poorer autodoping element than boron. One significant factor is vapor pressure. Arsenic "evaporates" more easily than boron. The exact nature of the autodoping differences between the elements have not been reported, but empirical data to be presented here demonstrate that the worst-to-best autodoping order of common silicon dopants is  $\text{As} \gg \text{B} > \text{P} > \text{Sb}$ .

The second source of dopant for autodoping is evaporation from the backside of the wafer. The amount of autodoping is proportional to the evaporation rate. This rate and the autodoping profile depend to first order on wafer dopant concentration  $N_0$ . The net effect is that the wafer backside supplies dopant to the epitaxial layer at a rate initially set by its concentration, evaporation rate, diffusivity, and temperature. The amount of dopant supplied then decreases slowly in time because of dopant-depletion effects on the wafer backside. The time variation is usually weak so that the backside appears as a relatively constant autodoping source. The solution to this boundary condition is simple. For a given set of growth conditions, the autodoping profile is constant and dependent only on initial wafer-backside doping. In a study [12] of intrinsic epitaxial layers ( $\text{SiH}_4$ ,  $1050^\circ\text{C}$ ,  $0.35 \mu/\text{min}$ ) grown on arsenic-doped wafers, the following empirical relation was derived:

$$N(\text{constant autodoping level}) = (2.5 \times 10^5) N(\text{backside}) \quad (17)$$

The constant autodoping levels were measured at 4 to  $7\mu$  from the original wafer surface, after the point at which the frontside evaporation and outdiffusion transients had died out.

With a general description of the three components of dopant movement into an epitaxial layer (outdiffusion and frontside and backside autodoping), a conceptual picture of autodoping can be drawn. Figure 11 shows that outdiffusion dominates nearest the interface, frontside evaporation effects become apparent as soon as the outdiffusion tail dies out, and backside evaporation dominates the autodoping profile farthest from the interface because the backside autodoping source remains relatively constant and the frontside source is continuously buried under growing silicon. Figure 11 is highly idealized; for example, the analysis does not consider lateral autodoping variations that include systematic worse autodoping at the wafer edges as a result of the backside source. Any of the three regions in Figure 11 may not be present

under certain conditions, (large outdiffusion tail may go completely to the surface of a thin epitaxial layer).

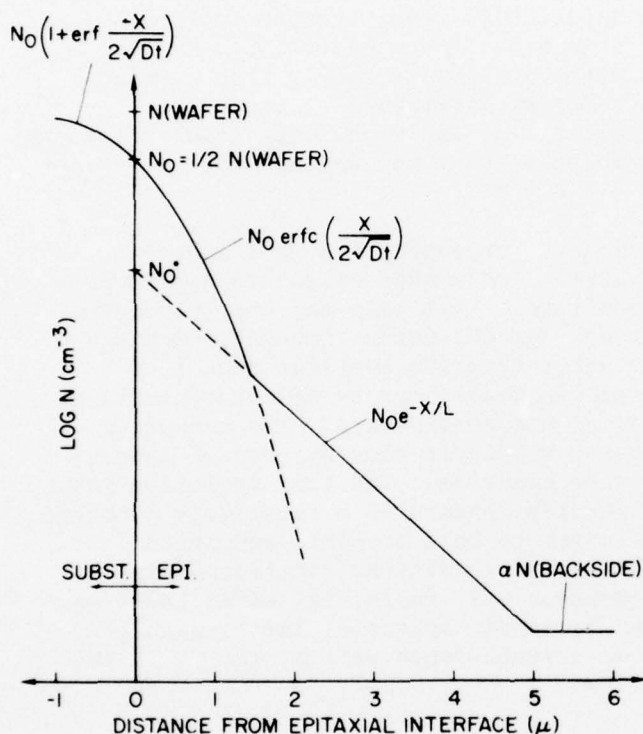


Fig.11. Conceptual diagram of autodoping and outdiffusion profiles.

**2.3.3 Time-dependent effects.** The above subsections have defined injection and autodoping effects primarily for the steady-state condition. Recent work has demonstrated practical means for obtaining a predefined doping profile by utilizing transient doping effects. A two-step process [13] using silane has achieved abrupt epitaxial interfaces by allowing the boundary layer vapor pressure  $P_g$  to decay with time after the growth of a first layer. The concentration in the first layer is reduced from the bulk value  $N_B$  to a value set by the ratio of loss coefficients  $\xi_{BI}$  from bulk to the first boundary layer, and  $\xi_{IE}$  from the second boundary layer to the epitaxial layer,

$$N_B^* = \frac{\xi_{IE}}{\xi_{BI}} N_B \quad (18)$$



Following this decrease in surface concentration, the vapor pressure decays to a second equilibrium value with an exponential time behavior. Subsequent epitaxial growth after the decay of  $P_g$  results in an abrupt doping profile.

A transfer-function characterization method has been reported that predicts profiles for time-varying injected dopant species [14]. Figure 12a is a block diagram of the epitaxial reactor as a system, the input is the gas flow as a function of time  $f(t)$ , and the output is the doping density profile in the epitaxial layer  $N(x)$ . All four blocks interact, With respect to the doping mechanism and despite such complexity, the reactor can be considered analogous to a linear system within limitations. The implication of this is that it is possible to obtain a transfer function of the reactor that relates the dopant gas-flow input  $f(t)$  to the doping profile output  $N(x)$  as shown in Figure 12b. After the transfer function has been determined, it is possible to calculate the dopant gas flow as a function of time required to achieve a desired dopant profile in an epitaxial film.

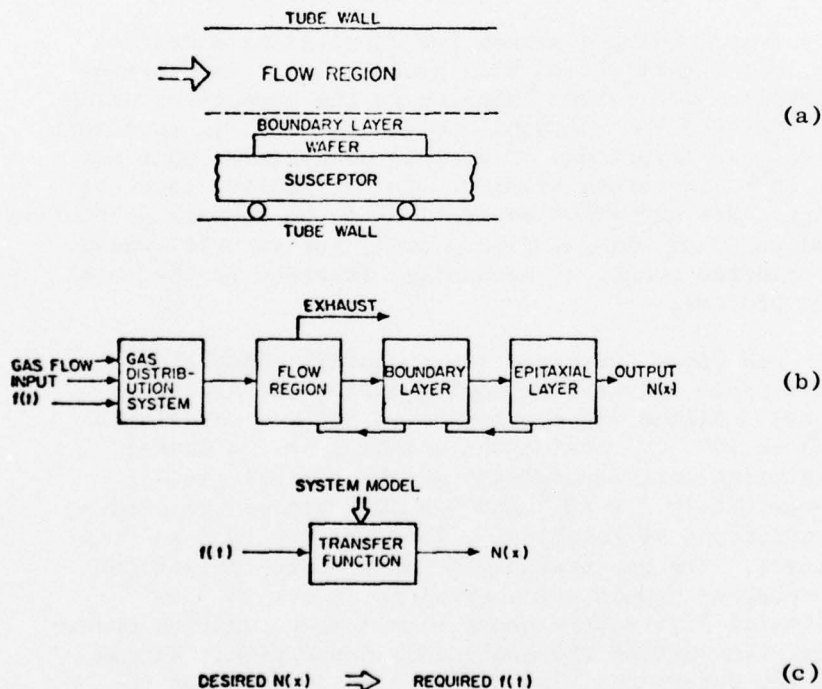


Fig. 12. Block diagram of reactor system.

- (a) Cross section of the reactor chamber
- (b) The reactor as a system
- (c) One transfer function relating the dopant gas-flow input  $f(t)$  to dopant concentration in the epitaxial film  $N(x)$

2.3.3a Transient response of the dopant incorporation mechanism. A linear system can be characterized by obtaining its transient response. After this response is known, it is a relatively easy task to determine the transfer function.

Although there are definite limits to this approach, it has been used successfully in several chemical systems. For example, diffusion-rate processes in catalytic reactors have been characterized by "admittance functions" analogous to ac electrical parameters [15]. The time-varying output-gas concentrations were related to the time variations of the input gases. Further work has considered diffusion through a boundary layer, adsorption on a surface, and diffusion into a solid [16]. Several of the same kinetic processes are present in our study of dopants in epitaxial layers; however, additional chemical processes are involved because the output is not a time-varying gas concentration, but a variation of the solid dopant concentration as a function of position in the deposited epitaxial layer.

In addition to providing a method for fabricating a desired dopant profile, this investigation will produce basic information concerning the various mechanisms involved in the dopant-inclusion processes. As indicated by Kobayashi and Kobayashi [17], transient studies may reveal the importance of various mechanisms that may not be apparent in steady-state studies. In particular, consideration of limiting cases may allow separation of the several mechanisms involved; dopant gas flow without film growth, for example, would involve only a selected number of mechanisms involved in the total epitaxial doping process.

The reactor was first optimized for a nominal deposition of approximately  $0.6 \mu/\text{min}$  and uniform doping during the entire deposition process. Silane was the source of Si, and deposition was accomplished at  $1070^\circ\text{C}$ . Arsine was selected as the dopant gas, and flow settings were determined for the typical partial pressure of approximately  $2 \times 10^{-6}$  and  $6 \times 10^{-6}$  atm, corresponding to dopant concentrations of roughly  $1 \times 10^{15}$  and  $3 \times 10^{15} \text{ cm}^{-3}$  in the epitaxial layer. The substrates were  $\langle 100 \rangle$ -oriented silicon wafers with phosphorous dopant concentrations in the  $10^{15} \text{ cm}^{-3}$  range. The epitaxial layers were grown with a step-function change in the dopant gas flow during the continuous deposition; during the deposition, the dopant gas flow was changed from one of the above described to the other to simulate the step input. Both the increasing and decreasing steps were used in these experiments.

The dopant profiles in the epitaxial layers were obtained by capacitance-voltage measurements on deep-depletion MOS structures and on planar and mesa p-n junctions. The thickness and dopant

concentrations in the samples were chosen to be compatible with the C-V technique. Spreading-resistance measurements and stacking-fault thickness determinations were used to confirm the capacitance-voltage measurements. Figures 13 and 14 are the resulting dopant profiles. To ensure that the experimental profiles were not limited by the resolution of the capacitance-voltage data-reduction technique, a theoretical capacitance-voltage curve was generated by solving Poisson's equation. The data-reduction program was then applied to this curve. The results revealed that the experimental profiles varied slowly compared to the resolution profile, indicating that the major features observed were not artifacts of the analysis technique.

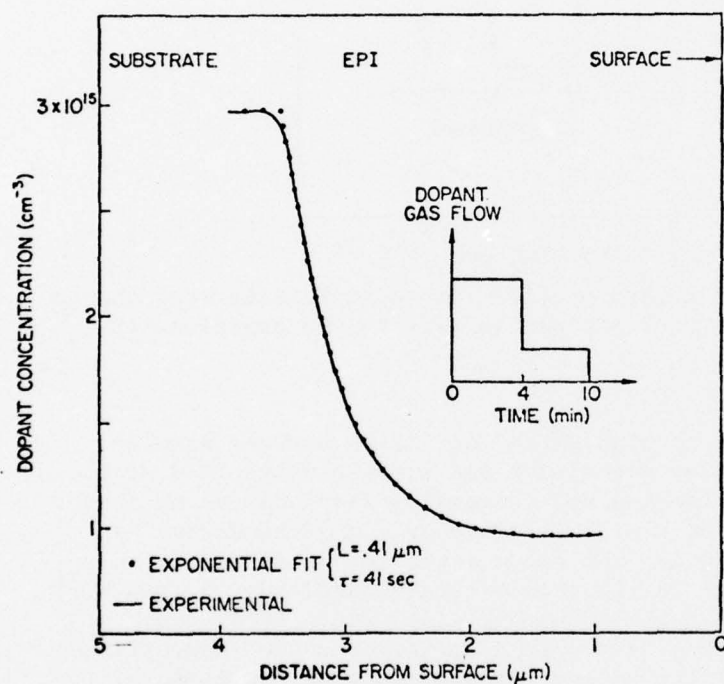


Fig. 13. Experimentally observed dopant concentration as a function of distance from the surface of an epitaxial film for a decreasing step change in the dopant gas flow. Also shown is an exponential fit to the experimental curve.

As can be seen in Figures 13 and 14, the transition from one dopant concentration to the other occurred in approximately  $1.2 \mu$ , corresponding to roughly 2 min. The heat cycling during the fabrication of the MOS and p-n junction C-V samples produced a square-root of  $Dt$  of only  $0.07 \mu$  because of the low diffusivity of the arsenic dopant in the epitaxial layer. Spreading-resistance data

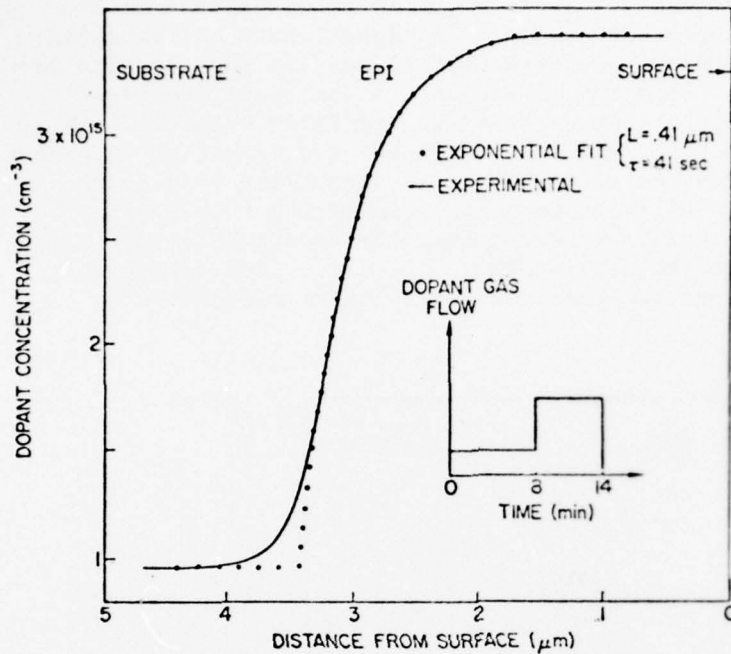


Fig. 14. Experimental dopant profile for an increasing step change in dopant gas flow and exponential fit to the experimental profile.

confirm that there is no significant deviation between samples measured after epitaxial deposition and after complete C-V sample fabrication. The increasing and decreasing steps reveal an abrupt onset of the transition region followed by a gradual decay. As seen in Figures 13 and 14, the decay curve can be fitted to an exponential curve with fairly good accuracy, and a decay length of  $0.41 \mu$  corresponds to a time constant of 41 sec. As a result, the transient response of the epitaxial factor can be approximated by a single exponential function, and the response is given by

$$H(t) = 1 - \exp\left(-\frac{t}{T_1}\right) \quad (19)$$

where  $T_1 = 40$  sec.

**2.3.3b System analysis.** After the transient response of a system has been characterized, it is possible to predict the output for a certain input. One of the simplest methods is to use the convolutional integral.

In a linear system, the output  $g(t)$  to an input  $f(t)$  can be calculated by convolving the input with the impulse response  $I(t)$ ,



$$g(t) = \int_0^{\infty} I(\tau) f(t - \tau) d\tau \quad (20)$$

The impulse response can be determined by taking the time derivative of the step response  $h(t)$ ;  $I(t) = \partial h(t)/\partial t$ . Because  $h(t) = 0$  for negative values of  $t$ ,  $I(\tau)$  is also zero for negative values of  $\tau$ . The lower limit of integration can be simplified, therefore, to

$$g(t) = \int_0^t I(\tau) f(t - \tau) d\tau \quad (21)$$

The limits of integration can be further simplified, depending on the form of the input. For example, if  $f(t) = 0$  for  $t < 0$ , then  $f(t - \tau) = 0$  for  $t < \tau$ , and thus the upper limit of the integration becomes

$$g(t) = \int_0^t I(\tau) f(t - \tau) d\tau \quad (22)$$

Equations (21) and (22) can be evaluated analytically or numerically through numerical integration.

Similar calculations can be performed in the frequency domain via the Laplace or Fourier transform. The advantage of the Laplace transform is that it is possible to draw analogs to electrical circuits; the advantage of the Fourier transform is that numerical methods are very efficient. In both techniques, repeated transforms are necessary to convert the information from the time domain to the frequency domain and then back to the time domain.

In the epitaxial reactor, differentiating Eq. (19) obtains

$$I(t) = \frac{1}{T_1} \exp\left(\frac{-t}{T_1}\right) \quad (23)$$

Because the growth rate  $G$  is constant in time, the doping density  $N(x)$  is

$$N(x) = G g(t) \quad (24)$$

By combining Eqs. (22), (23), and (24),

$$N(x) = \frac{G}{T_1} \int_0^{\infty} \exp\left(-\frac{\tau}{T_1}\right) f(t - \tau) d\tau \quad (25)$$

As noted earlier, the limits of integration can be simplified, depending on the type of  $f(t)$ .

2.2.3c Verification of the approach. In a series of experiments, the dopant gas flow consisted of an increasing step followed by a decreasing step, approximating a pulse in the input. Four pulse widths were used (4.3, 3, 1.8, and 0.8 min). The resulting doping profiles in the substrates were measured using the C-V techniques, and Figure 15 plots the results. For pulse-widths of 4.3 and 3 min, the resulting profiles appear to be a simple superposition of profiles obtained in Figures 13 and 14 because the pulse widths are longer compared to the system time constant (41 sec). When using shorter pulses of 1.8 and 0.8 min, however, the higher limit of doping was never reached, thereby indicating the limits of the deposition system in responding to arbitrary changes in the rate of dopant gas flow.

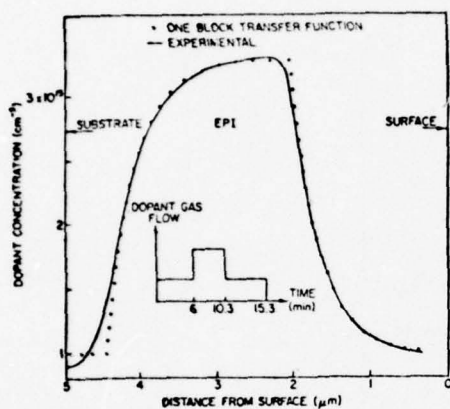
To verify the validity of the transfer-function approach, doping profiles were calculated using Eq. (25) for the four pulse inputs. The results are plotted in Figure 15. There appears to be excellent agreement between theory and experiments except at the onset of the high-to-low region. Even for the shortest pulse, where the pulse width of 48 sec is comparable to the system time constant of 41 sec, the model works with good accuracy.

In another experiment, the shape of the dopant gas-flow input function was a ramp followed by a step. The results of measurements and theoretical calculations are plotted in Figure 16 which, again, displays excellent agreement except for one discrepancy -- the initial and final values of the dopant gas flow are the same but are different for doping profiles in the epitaxial layer. This can be attributed to some mechanical malfunction in one of the flowmeters.

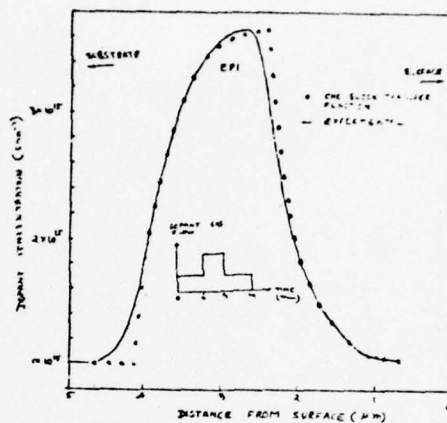
## 2.4 Summary for epitaxy

This section has defined several key problem areas in modeling silicon epitaxy. The kinetics of film growth and dopant inclusion have been discussed. First order models have been presented. In the final subsection recent results in transfer function modeling work in progress has been discussed.

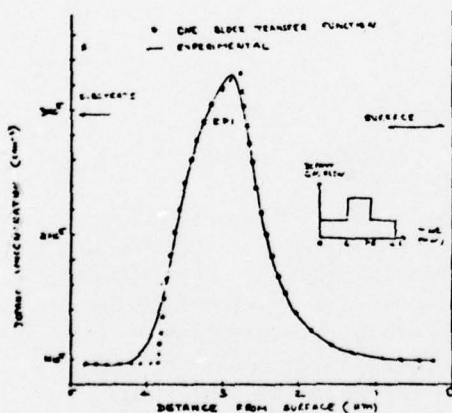
BEST AVAILABLE COPY



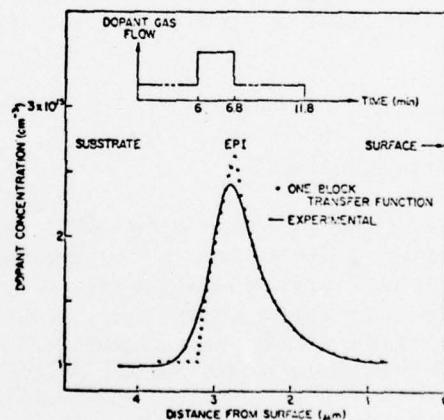
(a)



(b)



(c)



(d)

Fig. 15. Response of the reactor to pulse inputs in the dopant gas flow. The pulse width in time is  
(a) 4.3 min (b) 3 min (c) 1.8 min, and (d) 0.8 min.

BEST AVAILABLE COPY

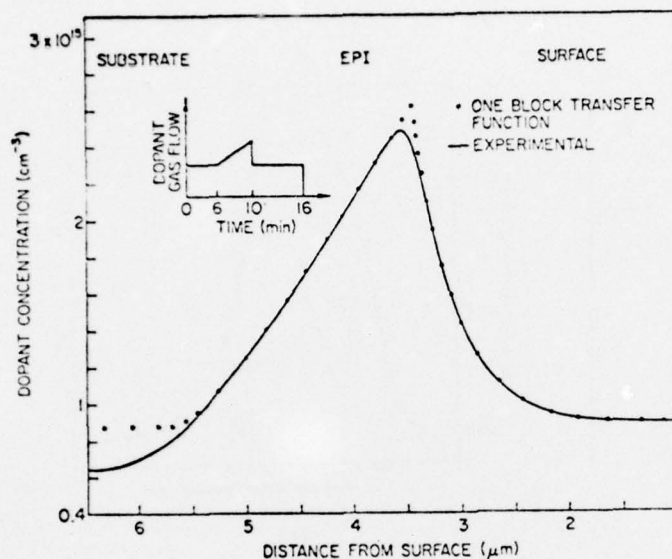


Fig. 16. Response of the reactor to a ramp followed by a decreasing step input in the dopant gas flow.

### 3. SILICON OXIDATION

#### 3.1 Introduction

Modeling the kinetics of silicon oxidation is well known [18]. The first-order model is based on the diffusion and surface reaction of a single oxygen species at the silicon interface. Present trends in the processing technology, however, are quickly outstripping the utility of the simple model. For example, concentration-dependent effects can change oxide thickness by as much as 300% for otherwise identical conditions. Low-temperature processing makes this effect even more pronounced. Partial pressures of oxygen, HCl, and other ambients also change growth parameters. Two-dimensional local oxidation with inherent strain-dependent effects is now a common technology tool which requires more extensive understanding of physics beyond the  $\text{SiO}_2$ -Si interface [41]. In addition, there are electrical alterations of the  $\text{SiO}_2$ -Si interface that result from physical properties. Deal [42] has recently reviewed this subject and it is clear that further work in this area is required. The presence of oxide and surface states can substantially change MOS threshold leakage, surface mobility, and overall device stability.



The multistream models for oxidation kinetics and two-dimensional dependencies will not be discussed here. It is anticipated that model development in these areas will benefit directly from other numerical modeling work that couples and conserves diffusing particles. The following discussion will be confined to problem formulations that have evolved as direct extensions of the first-order oxidation model [18]. This model will be reviewed and experimental results and interpretations will be considered for orientation, concentration, and ambient-dependent oxide growth conditions. In all cases, modifications amount to coefficient changes in the basic model.

### 3.2 The basic model

The first-order model solves for the oxide film growth by integrating a flux equation for oxygen as it crosses the silicon-oxide layer of thickness,  $x_o$ , and reacts at the silicon surface. Figure 17 is a schematic of the model, with the appropriate flux terms. According to Henry's Law, the equilibrium solid concentration is proportional to the bulk gas partial pressure,  $P_G$ ,

$$C^* = H P_G \quad (26)$$

where  $C^*$  is the maximum silicon-oxide concentration for a given  $P_G$  and  $H$  is the Henry's Law coefficient. Because we are treating non-equilibrium, the solid value is less than  $C^*$ . The flux,  $F_1$ , is determined by the difference in solid concentrations,

$$F_1 = h(C^* - C_o) \quad (27)$$

Here,  $C_o$  is the silicon-oxide surface concentration and  $h$  is the mass-transfer coefficient. The value of  $h$  in the solid can be related to the gas-transfer coefficient by

$$h = \frac{h_G}{HkT} \quad (28)$$

where  $h_G$  is the mass-transfer coefficient in the gas. The second and third flux terms shown in Figure 17 represent diffusive flux (Fick's Law) and the surface reaction. The diffusive flux is determined by the concentration gradient and the effective diffusivity  $D_{eff}$ ,

$$F_2 = D_{eff} \frac{\partial C}{\partial x} \approx D_{eff} \left( \frac{C_o - C_i}{x_o} \right) \quad (29)$$

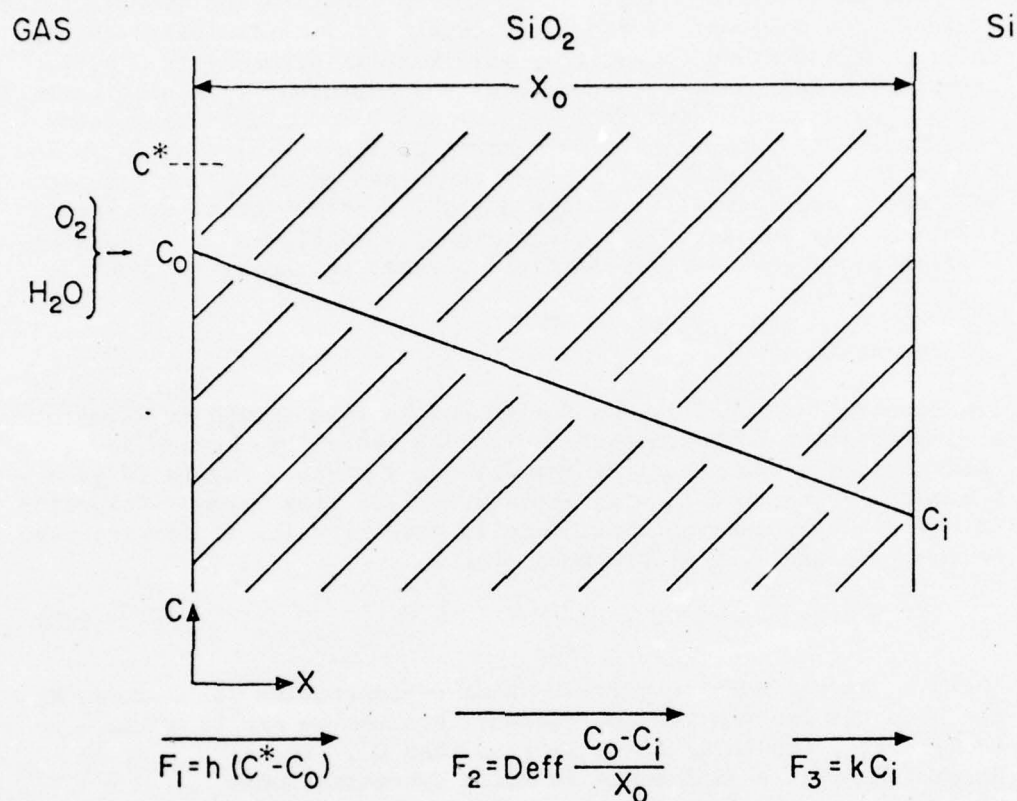


Fig. 17. Boundary and Flux conditions for the Gas-SiO<sub>2</sub>-Si system.

In this case,  $C_i$  is the interface value of the oxidizing species in the silicon oxide. The interface reaction rate is

$$F_3 = k C_i \quad (30)$$

where  $k$  is the surface-reaction rate constant for oxidation.

Using the condition at steady state ( $F_1 = F_2 = F_3$ ), one can solve for  $C_i$  and  $C_0$  in terms of  $C^*$ :

$$C_i = \frac{C^*}{1 + \frac{k}{h} + \frac{kx_o}{D_{eff}}} \quad (31)$$

and

$$C_o = \left(1 + \frac{kx_o}{D_{eff}}\right) C_i \quad (32)$$

Two limiting cases can be defined. Surface-reaction rate control occurs when  $D_{eff}$  becomes large (compared to the surface rate constant  $k$ ) and

$$C_i \approx C_o \approx \frac{C^*}{1 + \frac{k}{h}} \quad (33)$$

This condition implies that surface-reaction kinetics is the slowest, and hence dominant, effect. Mass transport, or diffusion control, occurs when  $k \gg D_{eff}/x_o$  and  $C_i$  approaches zero. In turn,  $C_o \approx C^* = Hk T C_G$  where  $C_G$  is the gas-phase oxidation concentration. Under these conditions, the flux toward the surface becomes

$$F = \frac{D_{eff}}{x_o} C^* \quad (34)$$

and the dominant effect is transport across the oxide layer.

To describe the rate of oxide growth, the flux equation at the interface can be written as

$$N_1 \frac{dx_o}{dt} = F_3 = \frac{kC^*}{1 + \frac{k}{h} + \frac{kx_o}{D_{eff}}} \quad (35)$$

where  $N_1$  is the number of oxidant molecules incorporated per unit volume ( $2.2 \times 10^{22}/\text{cm}^3$  for dry  $\text{O}_2$ , and  $4.4 \times 10^{22}/\text{cm}^3$  in a wet ambient). The following integral defines the relationship of  $x_o$  and  $t$ :

$$N_1 \int_{x_i}^{x_o} \left(1 + \frac{k}{h} + \frac{kx_o}{D_{eff}}\right) dx = kC^* \int_0^t d\tau \quad (36)$$

which results in

$$x_o^2 + Ax_o = B(t + \tau) \quad (37)$$

where

$$A \equiv 2 D_{\text{eff}} \left( \frac{1}{k} + \frac{1}{h} \right) \quad (38)$$

$$B \equiv \frac{2 D_{\text{eff}} C^*}{N_1} \quad (39)$$

and

$$\tau \equiv \frac{x_i^2 + Ax_i}{B} \quad (40)$$

The quadratic equation for  $x_o$  can be solved by the following limiting cases.

Case 1.

$$x_o \approx \frac{B}{A} (t + \tau) \quad \text{for } t + \tau \ll \frac{A^2}{4B} \quad (41)$$

and  $B/A$  is the "linear" rate constant.

Case 2.

$$x_o^2 \approx B(t + \tau) \quad \text{for } t + \tau \gg \frac{A^2}{4B} \quad (42)$$

and  $B$  is the "parabolic" rate constant.

Examination of the limiting forms indicates that the oxidation process in the parabolic domain is diffusion limited and, in the linear region, it is surface-reaction limited (generally,  $h \gg k$ ). Both regions should be directly dependent on the equilibrium concentration of oxidant in the oxide. Factors affecting the diffusion process should be most influential, therefore, over long oxidation times.

Experiments have indicated that, with an initially clean bare Si surface,  $x_i = 0$  for wet  $O_2$  oxidation, and an effective  $X_i \approx 200 \text{ \AA}$  is found for dry  $O_2$  oxidation (as a result of an initial phase of rapid oxidation by a different mechanism).



At the present time  $B$ ,  $B/A$ , and  $\tau$  are known only for (111)-oriented lightly doped conditions. Under these restrictions, these parameters can be expressed in the following form:

$$B = C_1 e^{-E_1/kT} \quad (43)$$

$$B/A = C_2 e^{-E_2/kT} \quad (44)$$

$$\tau = (X_i^2 + AX_i)/B \quad (45)$$

where

dry  $O_2$ :

$$\begin{aligned} C_1 &= 7.72 \times 10^2 \mu^2/\text{hr} \\ C_2 &= 6.23 \times 10^6 \mu/\text{hr} \\ E_1 &= 28.5 \text{ kcal/mole} = 1.23 \text{ eV/molecule} \\ E_2 &= 46.0 \text{ kcal/mole} = 2.0 \text{ eV/molecule} \end{aligned}$$

wet  $O_2$ :

$$\begin{aligned} C_1 &= 2.14 \times 10^2 \mu^2/\text{hr} \\ C_2 &= 8.95 \times 10^7 \mu/\text{hr} \\ E_1 &= 16.3 \text{ kcal/mole} = 0.71 \text{ eV/molecule} \\ E_2 &= 45.3 \text{ kcal/mole} = 1.97 \text{ eV/molecule} \end{aligned}$$

Orientation, the addition of a chlorine species, and heavy substrate doping have all been shown to affect  $B$ ,  $B/A$ , or both rate constants. The following sections discuss these individually.

### 3.3 Silicon crystal orientation effects

A log-log plot of oxide thickness vs oxidation time for the thermal oxidation of silicon in dry oxygen at temperatures ranging from 700° to 1200°C is shown in Figure 18. As expected, the difference in oxidation rate between (100)- and (111)-oriented silicon decreases gradually from 700°C (where the differences are on the order of 40%) to 1200°C (where the differences are less than 2% for all points) with the (111) oxidizing faster than the (100). It should be noted that, in the region below 100 Å at 700°C, the oxide thicknesses obtained for (100) and (111) silicon are essentially the same. Only after the oxide thickness exceeds 100 Å do the normal orientation differences appear. This observation suggests that, in the initial oxide growth regime at 700°C, the silicon surface

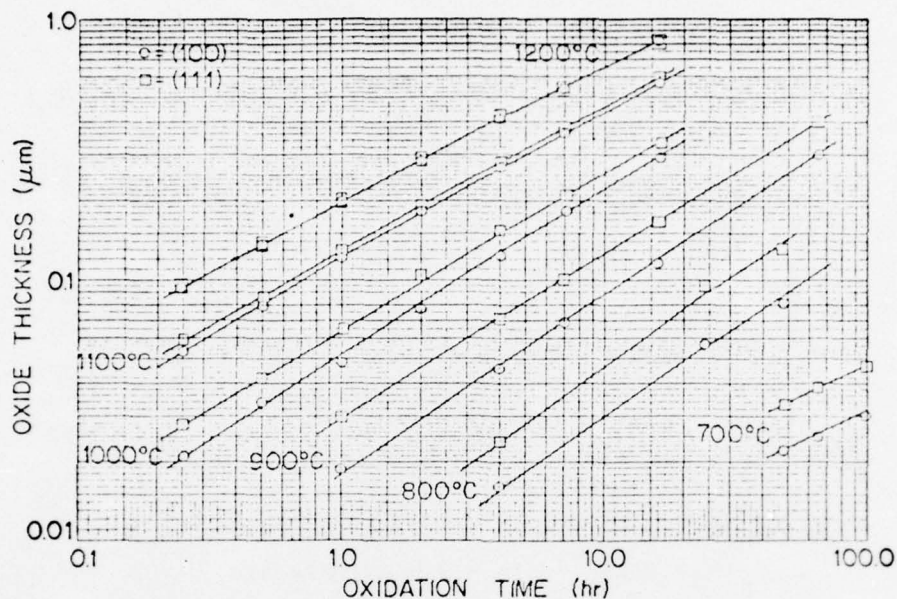


Fig. 18. Oxide thickness vs time for  $\langle 111 \rangle$  and  $\langle 100 \rangle$  silicon.

plays a minimal role. Such conclusions are consistent with previous data [19] obtained by Auger analysis of thin oxides grown between 200° and 800°C, which show that the hydration of the silicon surface plays a crucial role in silicon oxidation. The results can be of interest in the fabrication of MNOS devices.

The oxidation rate data were evaluated using the general relationship for the thermal oxidation of silicon given in Eq. (37). Because the parabolic rate constant  $B$  depends on the partial pressure of oxidant in the oxidizing ambient, the solubility of the oxidizing species in  $\text{SiO}_2$ , and the effective diffusion coefficient of the oxidizing species in  $\text{SiO}_2$  [18], there should be no variation of  $B$  with silicon orientation. On the other hand, the linear rate constant  $B/A$  involves the reaction rate constants at the  $\text{SiO}_2$  surface and at the silicon surface [18] so that any orientation dependence of the oxidation rate should appear in this term via the constant  $A$ .

Because the method of analysis utilized depends on the correction factor  $\tau$ , which is determined by extrapolation and is thus prone to some error, oxidation times at least three times greater than the  $\tau$  value for any set of oxidation conditions were generally used for the determination of B and B/A. In this way, any error in  $\tau$  should have little effect on the calculated values of B and B/A. The results of least-squares analyses of oxidation-rate data for (100)- and (111)-oriented silicon wafers using Eq. (37) are given in Table 4. It should be mentioned that the oxide thickness ( $x_i$ ) at zero oxidation time as determined by extrapolation of the  $x_o$  vs  $t$  curve to zero oxidation time, was found to be  $160 \pm 40 \text{ \AA}$  for all oxidation conditions. Table 4 demonstrates that, according to theory, there is essentially no difference in B for the two orientations, at least from  $1200^\circ$  to  $900^\circ\text{C}$ . Below  $900^\circ\text{C}$ , very long oxidation times ( $> 100 \text{ hr}$ ) become necessary to eliminate the effects of  $\tau$ , and the scatter observed was considerable. At  $700^\circ\text{C}$ , a value for B could not be obtained because a plot of oxide thickness versus time yielded a straight line, indicating that the parabolic contribution to the overall oxidation rate was negligible. The linear rate constant B/A, shows the expected orientation dependence, with B/A for (111) always being equal to or greater than that for (100). It should be noted that the kinetic parameters for (111)-oriented silicon in Table 4 are in very close agreement with those obtained by Deal and Grove [18]. Such agreement is remarkable when one considers the different oxidation conditions (humidity, gas quality, flow rates, furnaces, etc.) prevailing in two laboratories carrying out similar experiments 11 years apart.

Activation energies were obtained by fitting the data in Table 4 to an Arrhenius equation in the form of

$$k = k_o e^{\frac{-E_a}{kt}} \quad (46)$$

where  $E_a$  is the activation energy,  $T$  is the temperature in  $^\circ\text{K}$ , and  $k$  is a gas constant. Plots of B and B/A vs temperature are shown in Figures 31 and 32 in connection with the HCl data described later. This analysis obtained values of 1.3 eV (30 kcal/mole) and 1.2 eV (28 kcal/mole) for the activation energy of B for (100)- and (111)-oriented silicon, respectively, which agrees well with previously determined values for the dry thermal oxidation of (111)-oriented silicon [19, 20].

A similar analysis for the linear rate constant for the (111) orientation yielded a value of 2 eV (47 kcal/mole), which is in close agreement with the energy required to break a Si-Si bond [21]. Determination of the activation energy for B/A for (100)-oriented silicon, however, affords two choices. If the data from  $900^\circ$  to  $1200^\circ\text{C}$  are analyzed and the low-temperature points are neglected because of large scatter, a value of 2.5 eV (57 kcal/mole) is obtained -- an increase of  $\approx 25\%$  over that for (100). This

Table 4

RATE CONSTANTS FOR  $\langle 111 \rangle$  AND  $\langle 100 \rangle$  SILICON

Temperature (°C)	Orientation	$\tau$ (hr)	$A$ ( $\mu\text{m}$ )	$B$ ( $\mu\text{m}^2/\text{hr}$ )	$B/A$ ( $\mu\text{m}/\text{hr}$ )
1200	(100)	0.03	0.0399	0.0453	1.14
	(111)	0.03	0.0404	0.0458	1.13
1100	(100)	0.09	0.101	0.0247	0.246
	(111)	0.09	0.0845	0.0244	0.289
1000	(100)	0.35	0.195	0.00913	0.0467
	(111)	0.35	0.120	0.00956	0.0797
900	(100)	3.2	0.429	0.00332	0.00775
	(111)	1.2	0.214	0.00381	0.0178
800	(100)	10.0	0.441	0.000755	0.00171
	(111)	5.0	0.354	0.00119	0.00335
700	(100)	--	--	--	0.000222
	(111)	--	--	--	0.000348



increase was predicted by Ligenza from consideration of steric hindrance in the (100) and (111) planes of silicon during thermal oxidation [22].

On the other hand, if the data from 700° to 1200°C are analyzed, the 900°, 1100°, and 1200°C points could be considered as scatter from a line drawn parallel to the one for (111) orientation, passing through the 700°, 800°, and 1000°C points, thereby resulting in the same activation energy as (111)-oriented silicon. Indeed, some faith could be put in such an assumption, because the 700°C data give B/A directly from an  $x_o$  vs  $t$  plot as indicated above. One could argue, therefore, that the higher temperature analyses were in error due to the inaccuracy in determining A from a plot of  $x_o$  vs  $(t + \tau/k_o)$ . The slopes of these lines (B) are quite large; therefore, a small change in the slope would shift the intercept (A), and thus B/A, considerably. At present, it is not known which of the above alternatives is the correct one. In any case, the preceding discussion indicates that there has been little or no work reported since 1961 concerning the differences between oxidation rates and corresponding activation energies of (100)- and (111)-oriented silicon in dry oxygen.

### 3.4 Impurity doping effects

The effects of impurity doping levels on thermal oxidation rates are intimately connected with a widely encountered phenomenon in semiconductor processing -- namely, impurity redistribution. Figure 19 illustrates how redistribution and thermal oxidation interact.

As a thermal oxide is grown over a doped silicon substrate, redistribution of the impurity results. In the case of phosphorus, arsenic, and antimony, the dopant atoms tend to pile up at the surface, resulting in a higher surface concentration than background concentration ( $C_s \gg C_B$ ). In boron, the opposite effect takes place, resulting in surface depletion ( $C_s \ll C_B$ ).

Very heavily doped substrates ( $C_B \approx 10^{19}$ ), it has been observed [23] that for both phosphorus and boron, the oxidation rates can be substantially different (generally faster) than those observed on lightly or moderately doped substrates. With respect to Figure 19, the two parameters that have been correlated [23] with this increased oxidation are  $C_s$  (the dopant concentration in the silicon at the surface) and  $C_{ox}$  (the average impurity concentration in the oxide).

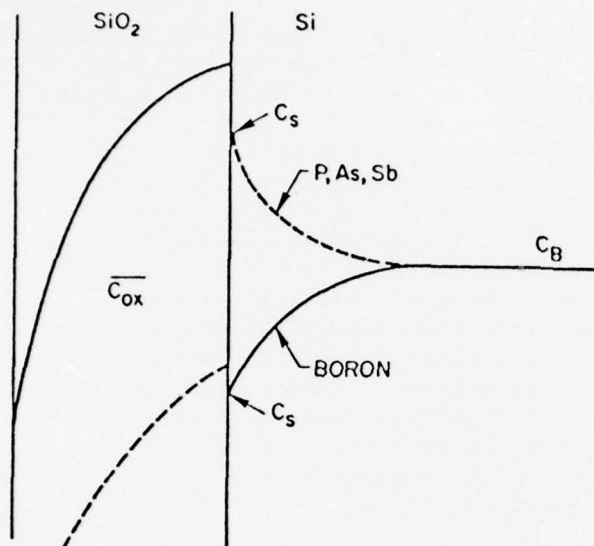


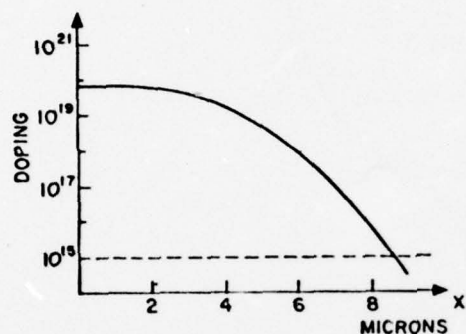
Fig. 19. Effect of redistribution on impurity doping profiles.

Intuitively, the effect of  $C_s$  is to reduce the amount of energy required to break Si bonds and thus to affect the surface reaction; it would thus be expected to influence the linear rate constant  $B/A$  and not  $B$ . The effect of  $C_{ox}$  is to change the diffusion constant for the  $O_2$  or  $H_2O$  oxidizing species in the  $SiO_2$ , and it would thus be expected to affect the parabolic rate constant  $B$ .

To study these enhanced oxidation rates in more detail, a large number of heavily doped wafers were prepared as illustrated in Figure 20. Because of the difficulty in purchasing wafers with doping levels  $> 10^{19}/cm^3$ , the samples were prepared by diffusion of phosphorus into standard lightly doped (111) substrates. The predeposition and drive-in schedules were chosen so that the diffused profiles were flat (within 10%) over the first  $2 \mu$  into the silicon. The drive-ins were done in  $N_2$  to prevent oxidation and hence redistribution during the formation of heavily doped layers.

Five types of samples were prepared with surface doping levels between  $5 \times 10^{19}/cm^3$  and solid solubility ( $\approx 3 \times 10^{20}/cm^3$ ), as indicated in Figure 20. The resulting diffused profiles were measured using spreading resistance and anodic sectioning techniques. Agreement between the two measurement techniques was excellent.

It is important to note that the doping concentrations tabulated in Figure 20 represent electrically active concentrations, not chemical concentrations.



SAMPLE	C <sub>s</sub>	
	SPREADING P	ANODIC SECTIONING
A	$5 \times 10^{19}$	$5.2 \times 10^{19}$
B	$7.2 \times 10^{19}$	
C	$1.8 \times 10^{20}$	
D	$2.8 \times 10^{20}$	$2.8 \times 10^{20}$
E	$3.1 \times 10^{20}$	$3.3 \times 10^{20}$

Fig. 20. Surface concentrations of diffused heavily doped samples.

Following preparation of the samples, a series of initial experiments were conducted to evaluate the magnitude of the enhanced oxidation effect over  $N^+$  regions. A typical result is shown in Figure 21. The horizontal scale is again an electrically active surface concentration. The data indicate approximately a three-to-one range in oxide thickness for these wafers which were oxidized simultaneously.

The choice of a low oxidizing temperature tends to maximize the enhanced oxidation rate for the common N-type impurities because, as explained above, they tend to pile up at the silicon surface. As a result, the dominant effect is on the reaction occurring at the Si-SiO<sub>2</sub> interface, and hence the linear rate constant B/A which dominates the overall reaction at low temperatures. It should be noted that low-temperature oxidation is becoming increasingly important in the semiconductor industry because of the trend toward larger diameter silicon wafers.

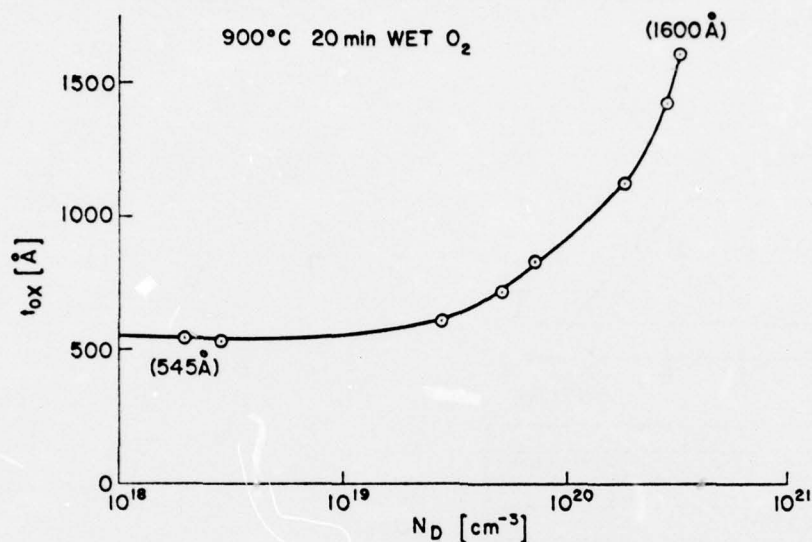


Fig. 21. Oxide thickness vs doping. Samples oxidized simultaneously.

Wet oxidation also tends to increase the effect observed in Figure 21 because there is more redistribution for wet oxides when N-type impurities are involved (Cs/Cb is larger for wet than dry oxides) [23,24].

Following these initial experiments, a more carefully designed series of oxidations were made to evaluate the enhanced oxidation over  $N^+$  regions under a wide variety of temperatures and ambient conditions. Typical of the results obtained are the data shown in Figures 22 and 23. The bottom curve (A) in each case is lightly doped ( $1 \times 10^{15}$ ) material, and the results agree with previously published data [18]. The upper curve (F) corresponds to a substrate doped to approximately solid solubility.

The following observations can be made about these data, even in the form shown in these figures.

- (a) The enhanced oxidation effect is more pronounced at



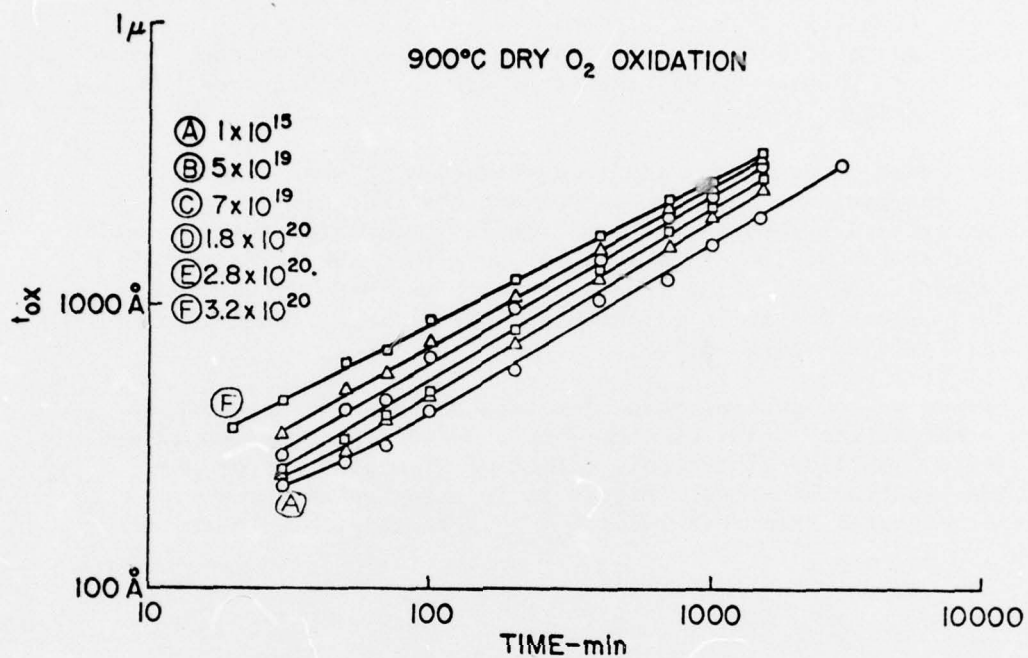


Fig. 22. Oxide thickness vs time for various doping levels at 900°C.

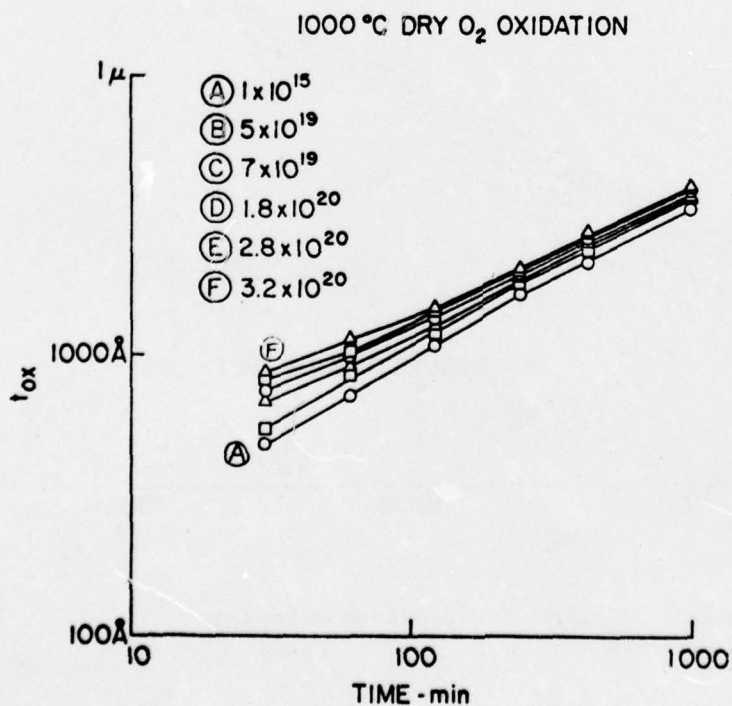


Fig. 23. Oxide thickness vs time for various doping levels at 1000°C.

lower temperatures (900°C) than at higher temperatures (1000°C).

- (2) These effects are also more pronounced for shorter times and thinner oxides than they are for longer times and thicker oxides.

Both of these observations are in agreement with our previously stated expectations; that is, N-type dopants that pile up at the silicon surface and segregate into the Si should affect the reaction kinetics at the Si-SiO<sub>2</sub> interface far more than they affect the diffusion of the oxidizing species through the SiO<sub>2</sub>. As a result, we would expect B/A to be affected and not B, in agreement with the observations stated above.

Based on the general oxidation relationship, we can consider from a theoretical point of view what the curves in Figures 22 and 23 should look like if the only effect of N<sup>+</sup> doping was on the surface-reaction kinetics. Figure 24 is a series of theoretical curves generated from this oxidation relationship. The various

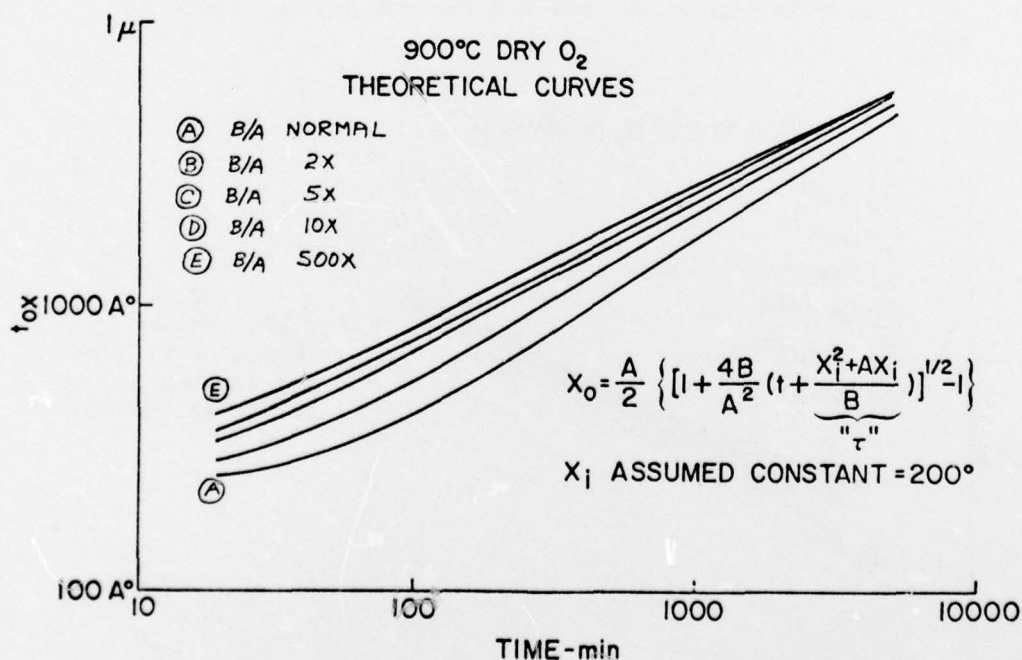


Fig. 24. Theoretical curves of oxide thickness vs time for various linear rate constants.

curves were generated for values of the linear rate constant  $B/A$  between the normal or lightly doped substrate value ( $2.8 \times 10^{-4}$   $\mu/\text{min}$  at  $900^\circ\text{C}$ ) and 500 times this value (corresponding to a much enhanced surface-reaction rate). The qualitative agreement between these theoretical curves and the experimental results in Figure 22 is apparent.

The analyses of these data in Figures 22 and 23 can be carried one step further by extracting linear and parabolic rate constants according to standard techniques [18]. The results for the  $900^\circ\text{C}$  oxidation are shown in Figure 25. The following conclusions can be drawn from these data.

- (1) The parabolic rate constant is essentially unchanged by the  $\text{N}^+$  substrate. This is in accordance with our expectations because most of the phosphorus segregates into the silicon.
- (2) The linear rate constant is virtually unchanged for doping levels  $< 5 \times 10^{19}/\text{cm}^3$ . Above this concentration  $B/A$  increases approximately one order of magnitude as the doping level is increased to the solid-solubility limit.

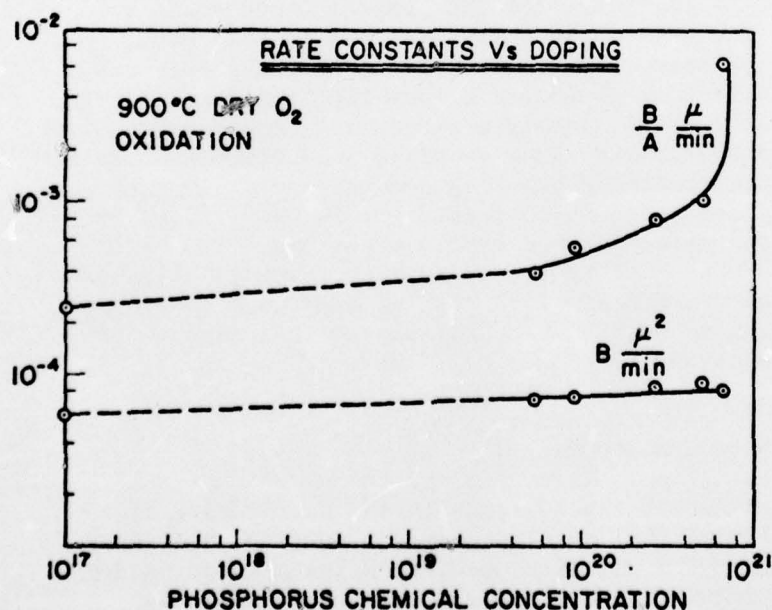


Fig. 25. Linear and parabolic rate constants vs chemical dopant concentrations at  $900^\circ\text{C}$ .

It should be noted that the horizontal scale in this figure has been corrected to a chemical phosphorus concentration in the substrate, rather than the electrically active concentration previously used. The chemical phosphorus concentration (and hence the percentage of the species electrically active in our diffused samples) was determined by sputtering Auger techniques by Johannesen et al. at Stanford University [25]. There is still some question concerning the absolute accuracy of the horizontal scale in Figure 25 because of the sensitivity limitations of the Auger technique. Independent measurements on these samples are currently being performed using SIMS techniques. These should resolve the question of chemical vs electrically active phosphorus concentrations in these samples.

The 1000°C extracted rate constants show a form very similar to Figure 25. Samples have also been oxidized at 1100° and 800°C, and the resulting oxide thicknesses are being measured. Completion of these data at the four temperatures will allow us to plot both B and B/A as a function of temperature and to extract activation energies for the rate constants as a function of substrate doping level.

The reported activation energy for lightly doped wafer for B/A, the linear rate constant, is approximately 46 kcal/mole [18]. This compares well to the energy required to break a Si-Si bond which is 42.2 kcal/mole [21]. The 900° and 1000°C data indicate that B/A becomes extremely large for the samples doped close to solid solubility. The activation energy for B/A in this case, therefore, approaches zero, thereby indicating that the reaction at the Si-SiO<sub>2</sub> interface is no longer a rate-limiting step at these doping levels; that is, it appears that the incorporation of dopant atoms in concentrations close to solid solubility so strains the lattice structure that bond breaking becomes extremely easy. Whether this simplified model is correct can only be verified by a better model of the molecular and atomic structure near the Si-SiO<sub>2</sub> interface. Such a model is necessary also for prediction of charge densities and is, therefore, a goal of our research program. We are also beginning to pursue it in the manner indicated at the beginning of this section.

### 3.5 Oxidation in HCl/O<sub>2</sub> mixtures

One of the most significant developments in the passivation of thermally grown silicon-dioxide films over the past several years has been the addition of a chlorine species during silicon oxidation. It has been demonstrated [26,27,28] that such additions result in improved threshold stability and increased dielectric strength. In addition, it has been observed that chlorine additions increase the rate of silicon oxidation [29,30,31], but extensive



data for widely varying oxidation conditions have not been reported. In this investigation, therefore, the thermal-oxidation kinetics of silicon in  $O_2/HCl$  mixtures is characterized as a function of oxidation temperature,  $HCl$  concentration, and silicon orientation; the results are compared to those obtained from silicon oxidations performed in a dry-oxygen atmosphere.

**3.5.1 Rate constants.** Log-log plots of oxide thickness vs oxidation time for the thermal oxidation of (100)- and (111)-oriented silicon in  $O_2/HCl$  mixtures at temperatures of  $900^\circ$ ,  $1000^\circ$ , and  $1100^\circ C$  are shown in Figures 26, 27, and 28, respectively. It is clear that the (111) silicon always oxidizes faster than does the (100). It can also be seen that the effect of the  $HCl$  addition is to increase the oxidation rate relative to oxidation in dry oxygen. In particular, a relatively large increase in the oxidation rate occurs with the initial 1%  $HCl$  addition. Subsequent additions have a somewhat smaller effect, but the overall rate is systematically increased. It can also be observed in these figures that the overall increase in oxide thickness for a particular oxidation time on increasing the  $HCl$  concentration from 0 to 10% is larger for (100)- than for (111)-oriented silicon. This effect may be related to the silicon-etching phenomenon. It should be noted that very few data

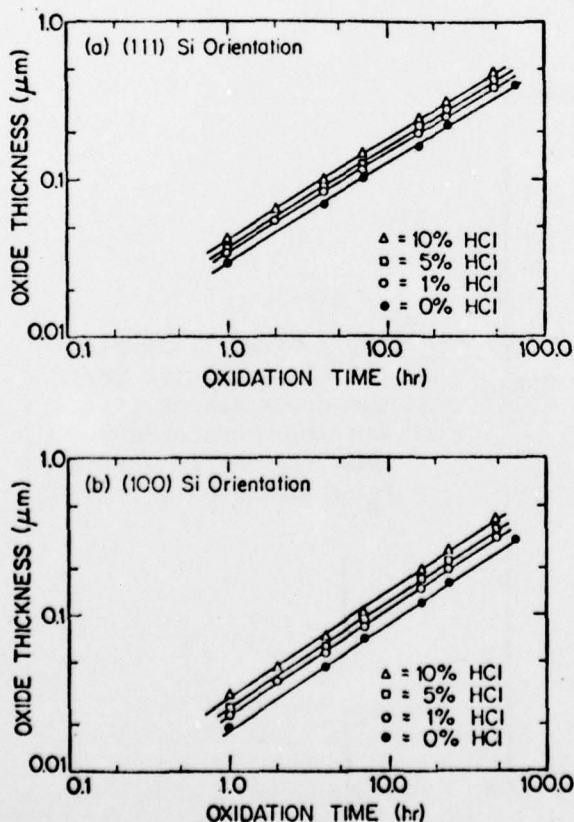


Fig. 26. Oxide thickness vs oxidation time for the oxidation of  $\langle 100 \rangle$ - and  $\langle 111 \rangle$ -oriented N-type silicon in various  $O_2/HCl$  mixtures at  $900^\circ C$ .

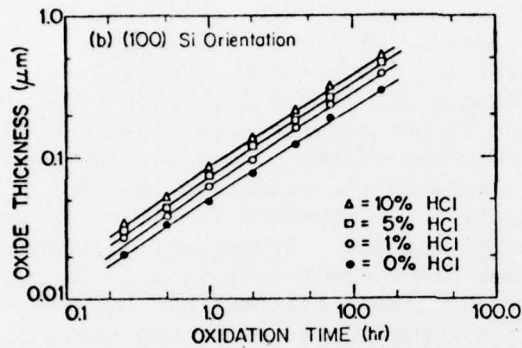
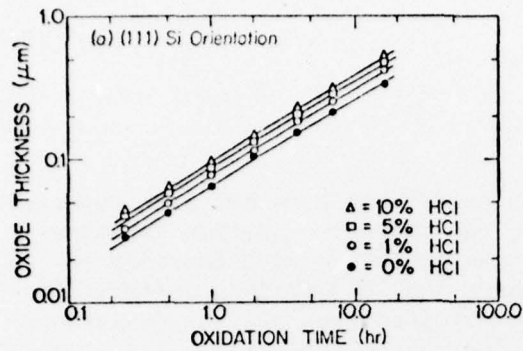


Fig. 27. Oxide thickness vs oxidation time for the oxidation of  $\langle 111 \rangle$  and  $\langle 100 \rangle$  oriented N-type silicon in various  $\text{O}_2/\text{HCl}$  mixtures at  $1000^\circ\text{C}$ .

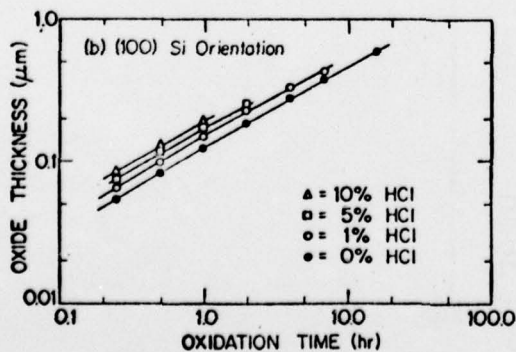
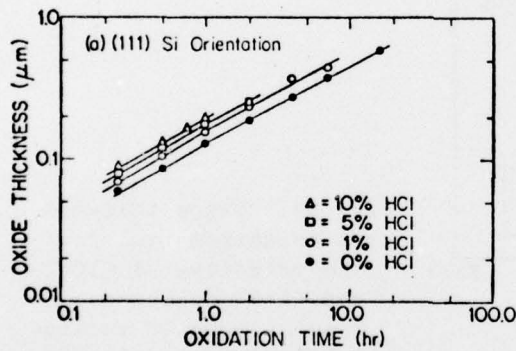


Fig 28. Oxide thickness vs oxidation time for the oxidation of 111 - and 100 -oriented N-type silicon in various  $\text{O}_2/\text{HCl}$  mixtures at  $1100^\circ\text{C}$ .

points are plotted for oxidations carried out at 1100°C with HCl concentrations greater than 1% because of silicon etching and oxide-bubble forming oxidation with O<sub>2</sub>/HCl mixtures at 1100°C [30,31,32,33].

To separate the effects of HCl on the parabolic B and linear B/A rate constants and to obtain some indication of the role HCl plays in silicon oxidation, Eq. (37) was utilized. During the determination of  $\tau$ ,  $x_i$  was assumed to be essentially constant at  $160 \pm 40$  Å for all oxidation conditions investigated. Although  $x_i$  should decrease with HCl addition due to water-vapor generation as per the reaction of O<sub>2</sub> and HCl



the extrapolations performed to determine  $x_i$  and thus  $\tau$  could not detect small changes in  $x_i$ . Nevertheless, because  $\tau$  depends on  $x_i$ , B, and B/A, a decrease in  $\tau$  was observed on HCl addition, probably in part as a result of water generation because  $x_i$  and, therefore,  $\tau$  are zero for oxidation in a steam ambient[18].

The results of least-squares analyses on the data in Figures 26, 27, and 28 are summarized in Figures 29 and 30 which are semilog plots of the effect of HCl concentration on the parabolic and linear rate constants, respectively. It should be noted that the rate constants generated via Eq. (37) and plotted in Figures 29 and 30 are effective rate constants in that they represent the combined effects of oxygen, water, and chlorine species on B and B/A.

Figure 29 shows that essentially no orientation effect is observed in the parabolic rate constant B, in accordance with theory; also, increasing the HCl concentration above 1% results in a linear increase in B (the plots are put on a semilog scale for convenience). The increase in B going from 0 to 1% HCl in dry oxygen is not as consistent among the three temperatures, however. For 1000° and 1100°C, a large increase in B due to a 1% HCl addition occurs, whereas this trend is not observed at 900°C. These observations are in agreement with previous work that revealed a linear increase of B with a 0 to 9% HCl addition at 900°C [31] and a large increase in B due to a 1% HCl addition at 1100°C [30]. Presumably, the large increase in B and the linear increase with subsequent HCl additions are the result of water generation as described in Eq. (47) because small amounts of water increase the thermal-oxidation rate of silicon in dry oxygen [34]. As pointed out by van der Meulen and Cahill [31], however, gas-phase thermodynamic equilibrium calculations indicate that the amount of water generated via Eq. (47) cannot account for the observed increase in the oxidation rate. This is consistent with the published results that a Cl<sub>2</sub> addition to a dry-oxygen atmosphere yields a considerably higher silicon-oxidation rate than

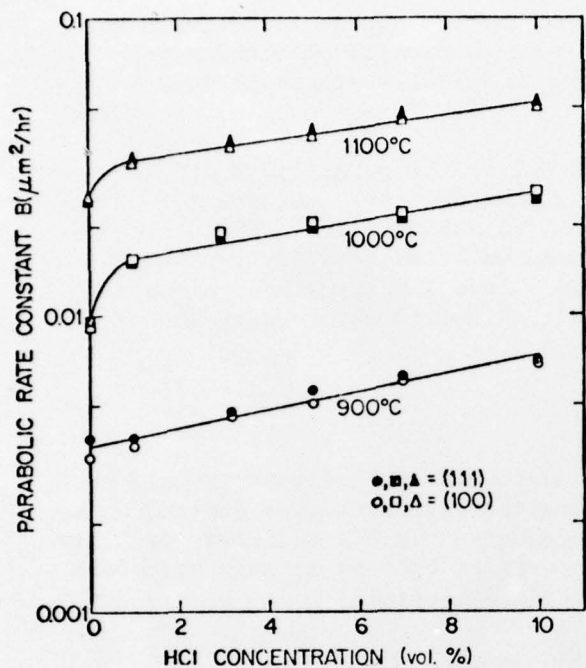


Fig. 29. Parabolic rate constant vs % HCl for <111> and <100> oriented N-type silicon at 900°, 1000°, and 1100°C.

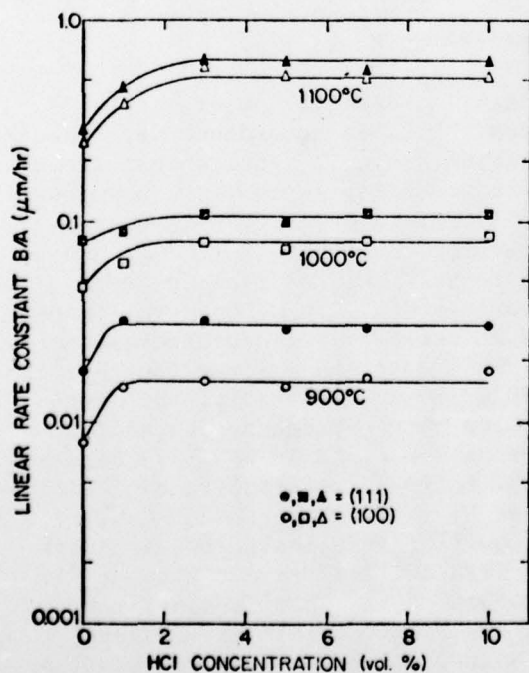


Fig. 30. Linear rate constant vs percent HCl for <111>- and <100>-oriented N-type silicon at 900°, 1000°, and 1100°C.



an equivalent HCl addition at 1150°C [34], suggesting that the chlorine species, rather than the water generated, may be primarily responsible for the increase in the oxidation rate at high temperatures. Because it is difficult to obtain Cl<sub>2</sub> which contains less than 3 ppm water, however, some effect, although small, would be anticipated from the water present.

In regard to the above argument concerning the amount of water generated via Eq. (47), thermodynamic calculations such as those in Ref. [31] give only the idealized gas-phase equilibrium conditions. The presence of a surface -- especially one such as SiO<sub>2</sub> which is useful for catalytic purposes -- could shift the equilibrium and thus alter the amount of water generated and incorporated into the oxide surface.

Some insight can be gained into the silicon-oxidation regime affected by water or chlorine [as generated via Eq. (47)] from consideration of the definitions of the parabolic (B) and the linear (B/A) rate constants. The definitions are as follows [18]:

$$B = 2 D_{\text{eff}} \frac{C^*}{N_1} \quad (48)$$

where  $D_{\text{eff}}$  is the effective diffusion coefficient,  $C^*$  is the maximum concentration of oxidant in oxide, and  $N_1$  is the number of oxidant molecules incorporated into a unit volume of oxide,

$$B/A = \frac{C^*}{N_1 \left( \frac{1}{k} + \frac{1}{h} \right)} \quad (49)$$

where  $k$  is the surface-reaction rate constant, and  $h$  is the gas-phase transport coefficient.

Inspection of these definitions and a comparison of Figures 29 and 30 reveal that the monotonic increase in  $B$  with HCl concentration is related to the effective diffusion coefficient  $D_{\text{eff}}$  because this term does not appear in the expression for  $B/A$ . It also appears that the rapid initial increase in  $B$  and  $B/A$  may be related to the solubility of the oxidizing species in the oxide film. Although the latter conclusion could be explained by water addition, this explanation would not account for the increase in  $D_{\text{eff}}$  because this parameter is known to decrease with water addition [18].

In light of the above arguments, the gradual increase of the parabolic rate constant with increasing HCl concentration could be partially related to a chlorine species because it has been

established that a higher concentration of chlorine is incorporated into the silicon-dioxide film as the HCl concentration and/or the silicon-oxidation temperature are increased [35]. Consequently, increasing the chlorine concentration may cause the  $\text{SiO}_2$  lattice to be strained (especially near the interface) thereby allowing diffusion of the oxidant to occur more easily and increasing the oxidation rate as observed in the oxidation of heavily boron-doped silicon [36]. Because the ionic radius of boron when substituted for silicon in a silicon lattice (which should be close to the radius of boron substituted for silicon in  $\text{SiO}_2$ ) is 0.88 Å [37], and the ionic radius of chlorine is 1.8 Å [38], it would be expected that the  $\text{SiO}_2$  lattice expansion would be even greater for chlorine as compared to boron. This speculation is also consistent with the previous observation that  $\text{Cl}_2$  additions result in larger silicon-oxidation rates than do HCl additions at high temperatures because more chlorine is apparently incorporated into the  $\text{SiO}_2$  with  $\text{O}_2/\text{Cl}_2$  than with  $\text{O}_2/\text{HCl}$  mixtures [35].

Figure 30 reveals a strong orientation effect on the linear rate constant  $B/A$ , which apparently decreases with increasing temperature. This observation was discussed in the previous section on orientation effects. As generally found for  $B$ , an initial rapid increase in  $B/A$  can also be observed when increasing the HCl concentration in the oxygen atmosphere from 0 to 1%; however, a further increase resulted in essentially no change in  $B/A$ . Although an explanation for these observations is not apparent, it is conceivable that the breaking of Si-Si bonds could be promoted by etching the silicon substrate which is known to occur with the use of HCl [30,31,32,33] to increase the linear rate constant. Increased HCl concentrations, however, should then further increase  $B/A$  unless an equilibrium between oxidation and etching is established.

Additional investigation of this phenomenon is required if we are to understand the mechanism involved. Preliminary results obtained by Deal with  $\text{O}_2/\text{Cl}_2$  oxidation atmospheres in the Fairchild Laboratory substantiate the above interpretation; relatively large increases in  $B/A$  caused by a  $\text{Cl}_2$  addition at 1100°C were observed, with considerably smaller increases noted for  $B$ .

**3.5.2 Activation energies.** Figure 31 is an Arrhenius plot of the parabolic rate constant  $B$  for the thermal oxidation of silicon in  $\text{O}_2$  and several  $\text{O}_2/\text{HCl}$  mixtures. Because essentially no orientation effect was observed for  $B$ , only the (111) orientation is plotted.

A least-squares analysis of the data for dry oxygen produced a value of 1.2 eV (28 kcal/mole), which agrees well with previously determined values for the thermal oxidation of silicon in dry

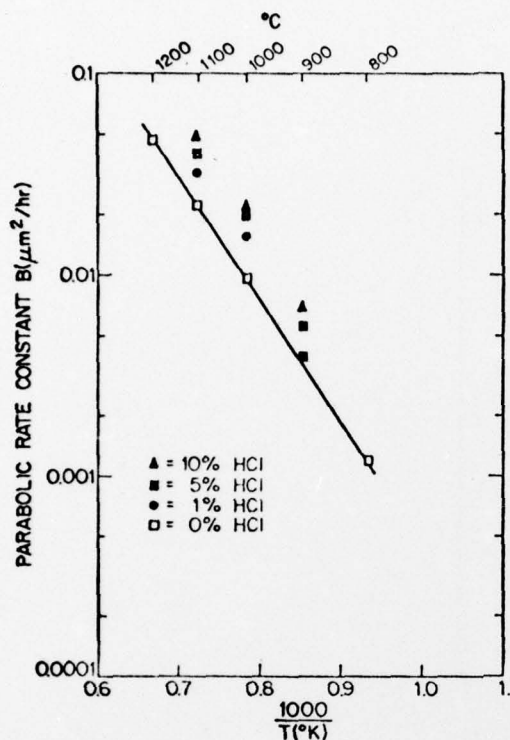


Fig. 31. Arrhenius plots of the parabolic rate constants for silicon oxidized in various  $O_2/HCl$  mixtures. Silicon orientation is  $\langle 111 \rangle$ .

oxygen [18, 39] and for the diffusivity of oxygen through fixed silica [40]. It can be seen that the HCl addition to the dry-oxygen atmospheres resulted in a convex curvature (relative to dry-oxygen oxidation) of the Arrhenius plot.

Figure 32 is an Arrhenius plot of the linear rate constant  $B/A$  for the thermal oxidation of silicon in  $O_2$  and several  $O_2/HCl$  mixtures. A least-squares analysis of the data for dry-oxygen (0% HCl) oxidation of  $\langle 111 \rangle$ -oriented silicon yielded a value of 2 eV (47 kcal/mole), which is in close agreement with the energy required to break a Si-Si bond [21]. Determination of the activation energy for  $\langle 100 \rangle$ -oriented silicon, however, affords two choices as explained in the previous section on orientation effects.

Similar to the parabolic rate constant, the Arrhenius plot of the linear rate constant for  $HCl/O_2$  mixtures (Figure 32) is curved, and the curvature is concave relative to dry-oxygen oxidation. Based on Eq. (47), it is not surprising that Arrhenius plots of the rate constants for oxides grown in HCl atmospheres should result in

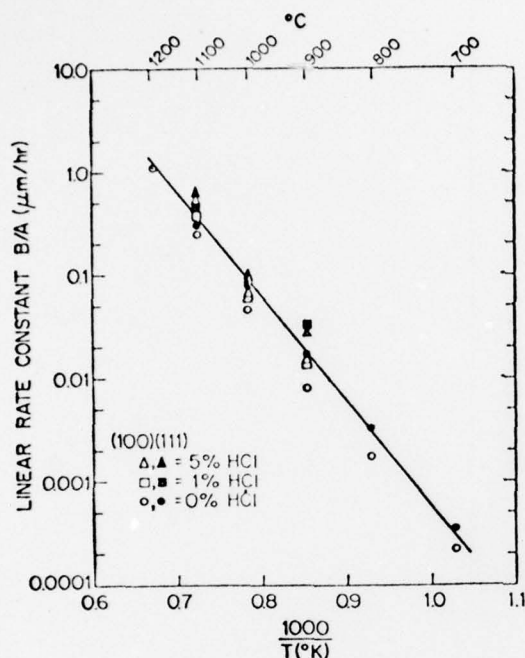


Fig. 32. Arrhenius plots of the linear rate constants for  $\langle 111 \rangle$  and  $\langle 100 \rangle$  oriented silicon oxidized in various  $O_2/HCl$  mixtures.

curved lines. It is apparent that more than one activation process is occurring (such as oxidation caused by oxygen and water vapor and several possible effects resulting from chlorine). As the oxidation temperature is changed, the relative importance of these activated processes may also change. It becomes necessary, therefore, to separate out the effects of water and chlorine on the silicon oxidation rate. Toward this end, experiments are being performed to investigate the oxidation rate of silicon in  $O_2/H_2O$  mixtures.

#### 4. CONCLUSION

In the previous section the fundamentals of silicon oxidation and first order process models have been presented. The subsequent discussions illustrate changes in the model coefficients which can account for changes in oxidation rates based on orientation, ambient and surface doping effects.



In both the epitaxy and oxidation sections the discussion has focused on two areas. First, the basic process models have been defined. Second, recent advances have been summarized which extend the range of application of the basic models to include state-of-the-art processing techniques. This includes programmable doping of epitaxial layers and ambient and surface effects during oxidation.

# REFERENCES

1. D.W. Shah, "Mechanisms in Vapour Epitaxy of Semiconductors," in Crystal Growth Theory and Techniques, Vol. 1, ed. by C.H.L. Goodman, Plenum Press, London, 1974.
2. T.I. Kamins, IEEE Trans. on Parts, Hybrids and Packaging (PHP-10), 4, Dec. 1976, p. 221-229.
3. M.L. Hammond and R.J. Gieske, "Hot Wall CVD -- Impact on the Industry," presented at Semicon, San Mateo, California, May 27, 1976.
4. T.J. Rodgers, "Advanced Integrated-Circuit Technology for Micro-power IC's," SEL-75-034, Ph.D. Dissertation, Stanford University, Stanford, California, Aug. 1975.
5. F.C. Eversteyn et al., J. Electrochem Soc. (117), 7, Jul. 1970, pp. 925-931.
6. R.F.C. Farrow, J. Electrochem. Soc. (121), 7, Jul. 1974, pp. 899-907.
7. H.C. Theuerer, J. Electrochem. Soc. (108), 7, Jul. 1961, pp. 649-653.
8. J. Bloem, J. Crystal Growth, (13/14), 1972, pp. 302-305.
9. J. Bloem, "Trends in the Vapor Deposition of Silicon," in Semiconductor Silicon 1973, The Electrochemical Society, Inc., Princeton, New Jersey, 1973, pp. 213-226.
10. A.S. Grove et al., J. Appl. Phys., (36), 3, Mar. 1965, pp. 802-810.
11. C.O. Thomas et al., J. Electrochem. Soc. (109), 11, Nov. 1962, pp. 1055-1061.
12. G. Skelly and A.C. Adams, J. Electrochem. Soc. (120), 1, Jan. 1973, pp. 116-122.
13. T. Ishii, K. Takahashi, A. Kondo, and K. Shirahata, J. Electrochem. Soc. (122), 11, Nov. 1975, pp. 1523-1531.
14. T.I. Kamins, R. Reif, and K.C. Saraswat, "Transient Response of Dopant Incorporation into Silicon Epitaxial Films," Extended Abstract No. 230, p. 601, 150th Electrochemical Society Meeting, Oct. 17-22, 1976, Las Vegas, Nevada.
15. P.F. Deisler, Jr. and R.H. Wilhelm, Industrial and Engineering Chemistry, (45), 1953, p. 1219.
16. J.B. Rosen and W.E. Winsche, J. Chem Phys. (18), 1950, p. 1587.
17. H. Kobayashi and M. Kobayashi, Catalysis Reviews - Science and Engineering (10), 1974, p. 139.
18. B.E. Deal and A.S. Grove, J. Appl. Phys. (36), Dec. 1965, pp. 377-3778.
19. J. Ruzyllo, I. Shiota, N. Miyamoto, and J. Nishizawa, J. Electrochem. Soc. (123), 26, 1976.
20. A.G. Revesz and R.J. Evans, J. Phys. Chem. Solids. (30), 1969, p. 551.
21. L. Pauling, The Nature of the Chemical Bond (3rd edition), Cornell University Press, Ithaca, New York, 1960.
22. J.R. Ligenza, J. Phys. Chem. (65), 1961, p. 2011.
23. B.E. Deal and M. Skalar, J. Electrochem. Soc. (112), Apr. 1965, pp. 430-435.
24. B.E. Deal, A.S. Grove, E.H. Snow, and C.T. Shah, J. Elec. Soc. (112), Mar. 1965, pp. 308-314.

25. J.S. Johannessen, W.E. Spicer, J.F. Gibbons, J.D. Plummer, and N.J. Taylor, "Observations of Phosphorus Pileup at the  $\text{SiO}_2$ -Si Interface," to be published.
26. R.J. Kriegler, Denki Kagaku (46), 1973, p. 446.
27. R.S. Ronen and P.H. Robinson, J. Electrochem. Soc. (119), 1972, p. 747.
28. C.M. Osburn, J. Electrochem. Soc. (121), 1974, p. 809.
29. R.J. Kriegler, J. Electrochem. Soc. (119), 1972, p. 388.
30. K. Hirabayashi and J. Iwamura, J. Electrochem. Soc. (120), 1973, p. 1595.
31. Y.J. van der Meulen and J.G. Cahill, J. Electron. Materials (3), 1974, p. 371.
32. R.J. Kriegler, Semiconductor Silicon, ed. by H.R. Huff and R.R. Burgess, The Electrochemical Society, Inc., Princeton, New Jersey, 1973, p. 363.
33. E.A. Irene, J. Electrochem. Soc. (121), 1974, p. 1613.
34. R.J. Kriegler, Y.G. Cheng, and D.R. Colton, J. Electrochem. Soc. (119), 1972, p. 388.
35. Y.J. van der Meulen, C.M. Osburn, and J.F. Ziegler, J. Electrochem. Soc. (122), 1975, p. 284.
36. B.E. Deal and M. Sklar, J. Electrochem. Soc. (112), 1965, p. 430.
37. Helmut F. Wolf, Semiconductors, John Wiley and Sons, Inc., New York, 1971, p. 199.
38. A.F. Wells, Structural Inorganic Chemistry, Oxford University Press, 1962, p. 68.
39. A.G. Renesz and R.J. Evans, J. Phys. Chem. Solids (30), 1969, p. 551.
40. F.J. Norton, "Nature" (171), 1961, p. 701.
41. T. Hirao, K. Kijima, and T. Nakano, Semiconductor Silicon, 1977, pp. 1005-1014.
42. B.E. Deal, Proc. of the Electrochem. Soc. Philadelphia, Pennsylvania, 9-13, May 1977.